MeerKAT's view of radio morphologies in the nearby X-shaped and dual-AGN system NGC 326

By

William Tabudi RASAKANYA

UNIVERSITY OF THE WITWATERSRAND, JOHANNESBURG

School of Physics
UNIVERSITY OF THE WITWATERSRAND

Submitted in fulfilment of the requirements for the degree
MASTER OF SCIENCE (MSC) IN PHYSICS
in the Faculty of Science, University of the Witwatersrand,
Johannesburg, South Africa.

May 5, 2023

Supervisors: Prof. Roger DEANE and Dr. Kshitij THORAT

UNIVERSITY OF THE WITWATERSRAND

Abstract

Faculty of Science
School of Physics

Master of Science (MSc) in Physics

MeerKAT's view of radio morphologies in the nearby X-shaped and dual-AGN system NGC 326

by William Tabudi RASAKANYA

Supervisors: Prof. Roger DEANE and Dr. Kshitij THORAT

Hierarchical structure formation in the Universe naturally predicts frequent galaxy mergers, and as a result, supermassive black hole mergers. A dual-AGN phase will then occur during the course of those mergers. Constraining the timescales spent at this stage provides predictions for supermassive black hole merger event rates and constraints on galaxy formation and evolution. Supermassive black holes at the centres of their host galaxies actively accrete matter in some systems, resulting in a production of radiation in a broad wavelength range, and in a fraction of those, radio-bright jets. The relativistic jets are usually paired and can span from parsec to megaparsec scales. A subclass of those have exotic radio morphologies, including the so-called 'X-shaped' sources. The study of such systems is important to better understand the intrinsic and extrinsic physical properties and feedback mechanisms influencing the evolution of radio jets, as well as the identification of exotic systems which may be used as physical laboratories. In this thesis, we present MeerKAT's first look at the prototypical, dual-AGN and previously characterised X-shaped system, NGC 326. The extended large-scale diffuse structure of NGC 326, revealed first by the LOFAR 144 MHz maps, is unveiled for the first time at GHz frequencies. Analysis of the MeerKAT L-band map, in combination with the LOFAR 144 MHz map, suggests that the production of the wings and the extended structure is a consequence of hydrodynamical backflows within the radio structure residing inside a merging cluster. Due to the high imaging fidelity, sensitivity, and dynamic range, the large-scale structure was able to be captured in the gigahertz observation, despite the low surface brightness and steep spectral index of the older plasma of the source. Detailed, multi-band imaging of nearby universe X-shaped sources such as this will directly assist in discerning the relevant physical drivers of the increasing number of exotic radio source morphologies being identified in SKA precursor and pathfinder surveys.

Declaration of Authorship

I, William Tabudi RASAKANYA, declare that the thesis, which I hereby submit for the degree of MSc in Physics at the University of the Witwatersrand, is my own work and has not previously been submitted by me for a degree at this or any other tertiary institution.

Signature:

Date: 5/05/2023

Acknowledgements

I would like to express my deepest gratitude to my supervisors, Prof. Roger Deane and Dr Kshitij Thorat. They have provided me with guidance & enlightenment; helpful comments; positive feedback; and were exceptionally patient. I am indebted to them and inspired to be better. I hope to work with both of you in the future.

I am extremely grateful to the South African Radio Astronomy Observatory (SARAO), who funded my studies and any equipment needed. I acknowledge the MeerKAT staff and observers, who provided the dataset used in this project. I also thank the Ilifu/IDIA cloud computing facility for providing the necessary tools to complete this project, and its staff for their helpful assistance.

Many thanks to Issac Magolego, for the lessons you have provided around spectral index map creations, the use of various software packages, and in general, being helpful whenever I sought guidance.

Thanks to Graham Lawrie, for being there with me from undergrad and through MSc. It was comforting and helpful having a fellow student and friend in the same space & mindset, and getting help from him with some admin requirements.

I would be remiss in not mentioning my family – especially my mother and my brother – who have always been supportive of me during my many years in academia and have always encouraged me to pursue what brought me happiness. I love you and I thank you.

Contents

List of Figures

List of Tables

List of Abbreviations

1GC	First **G**eneration **C**alibration
2GC	Second **G**eneration **C**alibration
3GC	Third **G**eneration **C**alibration
ACIS	**A**dvanced **C**CD **I**maging **S**pectrometer
AGN	**A**ctive **G**alactic **N**ucleus
CASA	**C**ommon **A**stronomy **S**oftware **A**pplications
CMB	**C**osmic **M**icrowave **B**ackground
CXO	**C**handra **X**-ray **O**bservatory
DD	**D**irection **D**ependent
DI	**D**irection **I**ndependent
EHT	**E**vent **H**orizon **T**elescope
FR–I	**F**anaroff-**R**iley Type–I
FR–II	**F**anaroff-**R**iley Type–II
FWHM	**F**ull-**W**idth **H**alf-**M**aximum
ICM	**I**ntra-**C**luster **M**edium
IDIA	**I**nter-University Institute for **D**ata **I**ntensive **A**stronomy
IPC	**I**maging **P**roportional **C**ounter
ISM	**I**nter **S**tellar **M**edium
KAT	**K**aroo **A**rray **T**elescope
LOFAR	**LO**w **F**requency **AR**ray
LoTSS	**LO**FAR **T**wo-meter **S**ky **S**urvey
MeerKAT	**Meer** **K**aroo **A**rray **T**elescope
MFS	**M**ulti-**F**requency **S**ynthesis
MOJAVE	**M**onitoring **O**f **J**ets in **A**ctive galactic nuclei with **V**LBA **E**xperiments
NED	**N**ASA **E**xtragalactic **D**atabase
NRAO	**N**ational **R**adio **A**stronomy **O**bservatory
NVSS	**N**RAO **V**LA **S**ky **S**urvey
PC	**P**lanetary **C**amera
PSPC	**P**osition **S**ensitive **P**roportional **C**ounter
PyBDSF	**Py**thon **B**lob **D**etector and **S**ource **F**inder
RFI	**R**adio **F**requency **I**nterference
RMS	**R**oot-**MeanS**quare
SKA	**S**quare **K**ilometre **A**rray
SMBH	**S**uper**m**assive **B**lack **H**ole
SNR	**S**ignal-to-**N**oise **R**atio
UHF	**U**ltra **H**igh **F**requency
VLA	**V**ery **L**arge **A**rray
VLBA	**V**ery **L**ong **B**aseline **A**rray
VLBI	**V**ery **L**ong **B**aseline **I**nterferometry
XRG	**X**-shaped **R**adio **G**alaxy
ZRG	**Z**-shaped **R**adio **G**alaxy

Chapter 1

Introduction

We present a study of a radio-loud source with an exotic morphology, which hosts a pair of active galactic nuclei at its cores, in this thesis. In this chapter, we explain what an active galactic nucleus is; delve into radio galaxies, the properties of radio jets, and the formation of exotic morphologies; then give an overview of the observed radio source and take an overview of the previous observations of the source.

1.1 Active Galactic Nuclei

An active galactic nucleus (AGN) is a small region typically found in the centre of a galaxy that comprises a supermassive black hole (SMBH) actively accreting matter. Matter falling into the black hole forms an accretion disk heated up by frictional interaction through differential rotation and viscosity. This heating, the resultant ionised media, and the presence of magnetic fields cause it to emit electromagnetic radiation in a broad wavelength range. Due to the immense gravitational potential energy of the black hole and conversion of a fraction thereof, this region can be highly luminous, even outshining its host galaxy in the case of quasars. Quasars are quasi-stellar objects – very bright and powerful AGNs in a broad range of wavelengths, whose accretion disk is (almost) perpendicular to the observer and outshine their host galaxy.

A black hole at the centre of a galaxy determines the stellar mass of the galaxy bulge through the AGN feedback, where the energy and radiation generated by accretion onto the massive black hole interact with the gas in the host galaxy. The flux of photons and particles produced by the AGN can remove the interstellar gas from the galaxy bulge and result in the termination of star formation and the active galactic nucleus, the latter being due to a lack of fuel for accretion (Fabian, 1999; Fabian, 2012, and references therein). In some cases, however, mechanical feedback has resulted in the enhancement of star formation (Bernhard et al., 2016; Ehlert et al., 2023).

Two major modes of AGN feedback that have been identified are radiative and kinetic. Radiative mode, also known as quasar or wind mode, operates in a galaxy bulge when the accreting black hole is close to the Eddington limit (maximum luminosity that a star or accretion disk can achieve when the outward radiative force equals the inward gravitational force; the balanced state being called hydrostatic equilibrium, van Marle, Owocki, and Shaviv, 2008). In radiative mode, the outward motion of gas and dust is either caused by the radiative pressure or AGN winds. Galaxies in this mode are usually optically thick and emit radiation at a broad range of wavelengths. The kinetic mode, which is also known as the radio jet or maintenance mode, usually occurs when the galaxy has a hot halo and the accreting black hole has powerful jets. Galaxies in this mode being active are usually optically thin and are observed easily at X-ray and radio wavelengths (Fabian, 2012, and references therein).

These AGNs sometimes include two radio jets typically along the axis of rotation and orthogonal to the plane of the accretion disk. These radio jets, in addition to the accretion disk, can also act as a dominant emission component of an AGN. One of the explanations for the nature of these jets is that relativistic particles are ejected due to the twisting of magnetic fields through differential rotation and frame-dragging effects in the vicinity of the black hole event horizon. While the details of the jet-launch mechanism are yet to be fully understood, it is expected that these conditions can lead to the rapid acceleration of hot and fast-moving ions away from the accretion disk. These jets become relativistic, and even ultrarelativistic, as the particles are accelerated to speeds close to the speed of light. Synchrotron radiation, with a wide range of wavelengths, is emitted as a result of accelerated charged ions spiralling around the magnetic field. Figure 1.1 presents an artist's concept of an accreting supermassive black hole with a perpendicular jet of twisting magnetic fields.

FIGURE 1.1: Artist's concept of a supermassive black hole with an accretion disk (orange/brown) and a helical jet (blue) perpendicular to the disk. Image credit: NASA/JPL-Caltech (2013).

The viewing angle of AGNs is known to impact their observational signatures strongly. The realisation of the viewing angle's impact on observational signatures has kicked off the "Unification Era" – the venture to explain different spectral exhibitions of AGNs with a single physical object (see Antonucci, 1993). However, it should be noted that not only does the viewing angle affect the observed properties, but so does the luminosity of the AGN, amongst other factors. AGNs that seem to transition from how they look challenge simple AGN Unification models and are explained by changes in the activity of the nucleus and not by their physical orientation with respect to our line-of-sight (Heckman and Best, 2014; Spinoglio and Fernández-Ontiveros, 2021). Nevertheless, the simple generalised model can be used to group the different sources as it is true to an extent. This so-called 'AGN zoo' described by the unified model includes blazars (AGNs with relativistic jets directed toward us); quasars (AGNs that outshine their host galaxies); Seyferts 1 and 2 (Spiral galaxies with bright nuclei), radio-quiet quasars; and radio galaxies (Fanaroff Riley Types I and II, FR–I and FR–II (Fanaroff and Riley, 1974)) (radio loud, flat spectrum sources). The last is most relevant to this project and is described in more detail in the next section.

1.2 Radio Galaxies

Radio galaxies are a class of active galactic nuclei that are highly luminous at radio frequencies. The structure of such sources consists of a core and a pair of active and collimated relativistic jets (if still active), as well as the defining features of large radio lobes, where the inner jets terminate(d). The lobes are giant regions of radio emission extending far from the host galaxy (Adams et al., 2004). The radio emission mechanism of this class of AGNs is dominated by synchrotron radiation from the core to the lobes, as magnetic fields pervade throughout the jets.

Since the discovery of the structure of Cygnus A in radio wavelengths (Jennison and Das Gupta, 1953), radio sources have been observed at wide ranges of frequencies, from MHz to hundreds of GHz frequencies. Rees (1971) found that double radio sources were seemingly powered continuously by jets ejected from their nuclei. Earlier, Rees (1966) had proposed that radio-loud quasars had relativistic motion, which caused the observed rapid radio variability. These relativistic motions produce superluminal motions – the apparently faster-than-light motions.

This discovery was critical in the unification of radio quasars with flat spectra. In fact, relativistic beaming is responsible for the observation of synchrotron spectra in the first place. The high observed masses of relativistic electrons, $m = \gamma m_e$, reduce their accelerations and orbital frequencies to low values, which in turn reduces the frequency of emitted radiation. Relativistic beaming turns the low-frequency sinusoidal radiation into high-frequency spikes in the frame of the observer (Condon and Ransom, 2016).

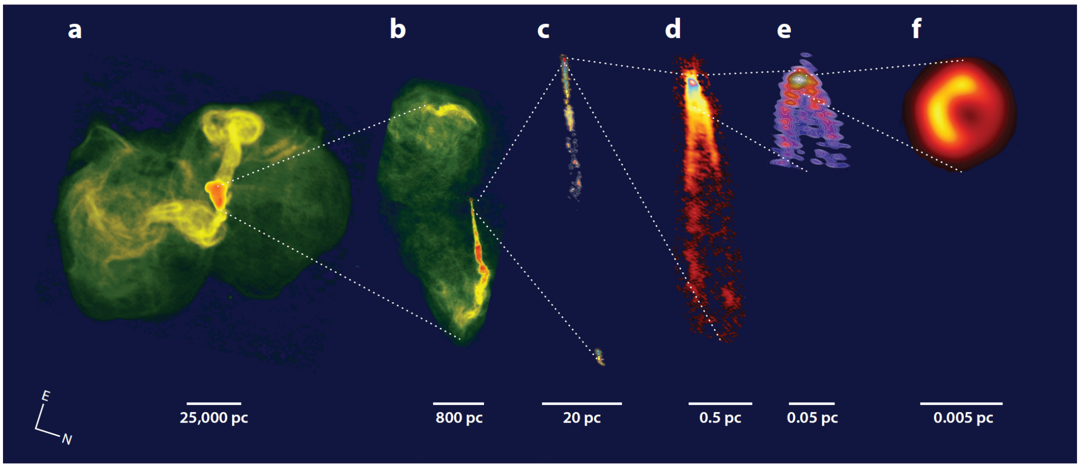

FIGURE 1.2: Reproduced from Blandford, Meier, and Readhead (2019) Figure 1. A montage of M87 radio images through various scales. The FR–I radio jets are shown to extend to kpc scales in (a). The effects of relativistic beaming can be seen in images b-d, where one of the jets is much more visible than the other. Image (e) shows the jet launching from the supermassive black hole and shows the unique morphology of the jet. Image (f) presents the first direct image of the shadow of the black hole. The images were taken with the following telescopes: (a) NRAO, 90-cm VLA; (b) NRAO, 20-cm VLA; (c) NRAO, 20-cm VLA VLBA; (d) NRAO, 7-mm VLBA; (e) 3-mm global VLBI network; (f) 1.3-mm Event Horizon Telescope.

1.3 Radio Jet Morphology

In order to attempt to explain various observed radio jet morphologies, we must first explain the nature of the radio jets. Jets produced by AGNs have been observed on a multitude of scales, from $\lesssim 1$ AU to $\gtrsim 1$ Mpc. Naturally, throughout the various extensions, the extrinsic and intrinsic conditions will differ. Three distinct jet scales have been distinguished on loosely defined scales. They consist of black hole, galaxy and lobe jets.

1.3.1 Black hole jets

These extend from the gravitational radius of the black hole, r_g, to the radius of influence of the black hole, R_{inf}. The black hole potential dominates the region, and this is where there is an inflow of matter to the accretion disk and outflow from it. Very Long Baseline Interferometry (VLBI) studies are able to capture these relatively small regions.

The gravitational radius of the black hole is defined by the equation

$$r_g = GM/c^2, \tag{1.1}$$

where G is Newton's Gravitational constant, M is the mass of the black hole and c is the speed of light. Similarly, the black hole's sphere of influence is defined by the equation

$$R_{inf} = GM/\sigma^2, \tag{1.2}$$

where σ is the one-dimensional central stellar bulge velocity dispersion.

Most VLBI observations are still restricted to scales of the black hole sphere of influence radius, R_{inf}, or larger of the target sources; thus, our understanding of radio emission on small scales relies on very few studies. Therefore, we summarise the results of an M87 study at its black hole jet scale and infer the physics at this scale. Walker et al. (2018) imaged the innermost jet of galaxy M87 using 50 *Very Long Baseline Array* (VLBA) 43 GHz observations (Figures 1.2 (d) and 1.3). The resolution, hence, was about $60 \times 120\ r_g$ of the SMBH. Some of the major results of their study are:

- wide-opening angle jet base with edge-brightened structure;
- overall parabolic jet shape with regions of rapid expansion and recollimation;
- counter-jet seen with a similar structure to the main jet; however, its brightness drops rapidly with distance, presumably as a result of Doppler boosting;
- in the inner 0.5 to 2 milliarcseconds (mas), a region of acceleration is observed;
- superluminal motions observed with apparent speeds from under 0.5 c to over 2 c; and
- helical magnetic fields are revealed close to the core by polarisation observations.

The *Event Horizon Telescope* (EHT) study of the M87 black hole at 230 GHz (Event Horizon Telescope Collaboration et al., 2019) revealed the shadow of the black hole and provided evidence that the jet is formed close to said massive black hole (Figure 1.2 (f)). Blandford, Meier, and Readhead (2019) summarised that the high speed of relativistic jets is produced slowly over a large distance (thousands of black hole radii) in FR–I sources.

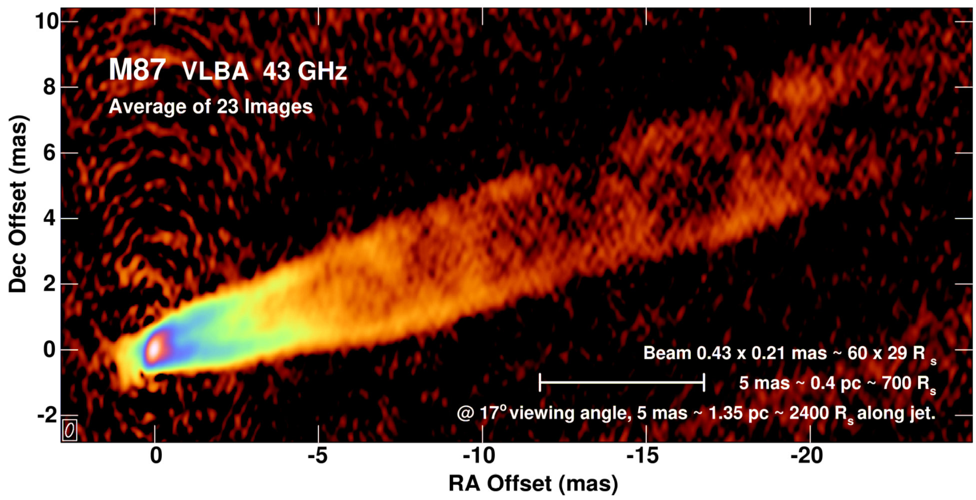

FIGURE 1.3: This is reproduced from Walker et al. (2018). Black hole jet image of M87 produced from 43 GHz VLBA observations. The angular and linear scales are indicated with the assumption that the jet is oriented 17° from line-of-sight. Shown in the lower left corner is the beam with a resolution of 0.43×0.21 mas, elongated in position angle –16°.

1.3.2 Galaxy jets

The galaxy jets carry the mass, energy, momentum and magnetic flux from the black hole and its accretion disk to the radio lobes (Blandford, Meier, and Readhead, 2019). Their interactions with the environment and their radiation losses provide for their observations. We use the scale set by Blandford, Meier, and Readhead (2019) and scale these jets from the black hole sphere of influence radius, R_{inf}, to the first 10% of the extent of the lobe, R_{lobe}.

Observational work on radio sources has revealed essential information about galaxy jets:

- The observed one-sided jets of kpc scales are a result of Doppler beaming (Garrington et al., 1988; Laing, 1988). Intrinsically, if the jets are two-sided and relativistic on both sides, then the one closer to us appears brighter due to Doppler beaming. Detailed polarisation observations would show that the lobe with the one-sided jet is less depolarised than the other, which is argued to be the result of Faraday rotation – nearer jet emission goes through less magnetoionic medium than the other, which causes differential Faraday rotation and thus, depolarisation.

- Furthermore, the observational work reveals that steep-spectrum jets ($-1.0 \leq \alpha \leq -0.5$ between 200 MHz and 5 GHz) originate from compact flat-spectrum ($\alpha \geq -0.5$) cores (Readhead et al., 1978).

- The features of jets are seen to move along the jets at superluminal speeds (Lister et al., 2019).

The *Monitoring Of Jets in Active galactic nuclei with VLBA Experiments* (MOJAVE) group (Lister et al., 2019) has studied 409 radio-loud AGNs using 15 GHz VLBA data spanning 22 years (1994 August 31 – 2016 December 26). The goal was to understand a blazar population by characterising the jet properties of a flux-density limited sample. We summarise some of the results of their study:

- 382 jets of the sample had a bright feature that could be tracked over five epochs. Evidence of accelerated motion at the 3σ level was found in 59% of the jet features.

- They confirmed that characteristic jet speeds are related to the underlying jet flow and that the speeds of jet features lie within $\pm$ 40% of the characteristic speed.

- They found 55 features in 42 jets with unusually slow pattern speeds, at least 10 times slower than the fastest feature, and that most of these lie within 4 pc (projected) of the core feature.

- After the examination of the maximum apparent jet speed distribution, they found it to peak at low values. Only a few speeds were above 30c. They concluded that, due to their survey not measuring instantaneous speeds above 50c and that Doppler-biased samples should contain the fastest jet speeds in the parent population, the distribution of jet Lorentz factors are not single-valued but rather have a power law distribution and are weighed towards low Γ (bulk Lorentz factor).

- They found a strong correlation between apparent jet speed and synchrotron peak frequency (ν_p). The highest jet speeds were found in AGNs with low ν_p values.

These observations surrounding galaxy jets, thus, reveal that highly relativistic jet bulk motions are superluminal and that the jets leave the radio source at high bulk relativistic speeds.

For FR–IIs at hundreds of kpc scales, there is neither evidence of these high bulk speeds nor is there evidence for a required strong deceleration to explain the different speeds at pc and kpc scales. This is explained by the jet being structured, with the emission seen on kpc scales coming from slower components, whereas most of its energy is being carried by the relativistic outflow. The jets of FR–II sources come out of their nuclei with mildly relativistic speeds and with a considerable amount of their initial power.

The situation is different and plain when it comes to the FR–I radio galaxies. One-sided on small scales but two-sided on large scales (such as M87 in Figure 1.2), they appear to have bulk deceleration if we are to attribute the sidedness feature to Doppler boosting. Laing and Bridle (2014) modelled the kpc-scale synchrotron emission from jets in 10 FR–I sources using the VLA and found that the jets initially have outflow speeds of $\sim 0.8c$ and then decelerate to sub-relativistic speeds where they stay constant. The deceleration is faster at the edges than on the axis. A sizable amount of the energy of the jets is dissipated at recollimation shocks near R_{inf}.

1.3.3 Lobe jets

This is the terminating part or stage of the jets where lobes of radio emission are inflated and, in some cases, backflows are observed. These vary depending on the nature of the jets, i.e. whether they are of Fanaroff-Riley type I or II. The outflows from the radio lobes form various morphologies on hundreds of kpc or even Mpc scales (such as the case of a giant radio galaxy, 3C 236).

The Fanaroff-Riley classes (Fanaroff and Riley, 1974) distinguish radio galaxies based on the relation between the positions of the high brightness regions to the low brightness ones and the luminosity of radio sources. Two such classes emerge from this definition, where those with brighter spots closer to the nucleus, have lower-powered jets and have a subsequent reduction in brightness towards the lobe edges, hence called edge-darkened, are Fanaroff-Riley type I (FR–I) (Fig. 1.4a); and those brighter in radio luminosities than their counterparts and have higher-powered jets with edge-brightened lobes, are Fanaroff-Riley type II (FR–II) (Fig. 1.4b).

The energy carried by the jets that is not lost in black hole or galaxy jets reaches the lobe jets and lobes themselves, where it is emitted. Leahy and Williams (1984) performed numerical simulations of the standard jet model of radio sources. They revealed that if a high Mach number jet flows into an ambient medium much denser than the jet, a 'cocoon' of jet material will be formed between the jet and the confining medium. If the jet is much less dense than the impacted medium, then the jet-shock speed will be less than the jet speed, from one-dimensional ram-pressure arguments. The continuous supply of jet material to the jet shock where post-jet shock material is rapidly decelerated results in most of the kinetic energy of the jet material getting converted to thermal energy at the shock and spreads the post-jet material away from the jet. The pressure in the inflated hotspot accelerates the material in the lobe toward the centre, thereby producing a backflow. However, if the density of the jet exceeds that of the ambient medium in which it collides, then little energy is lost and the post-jet material trails behind the jet shock and continues to move forwards. Thus, no bright hotspots or backflows are produced in this case.

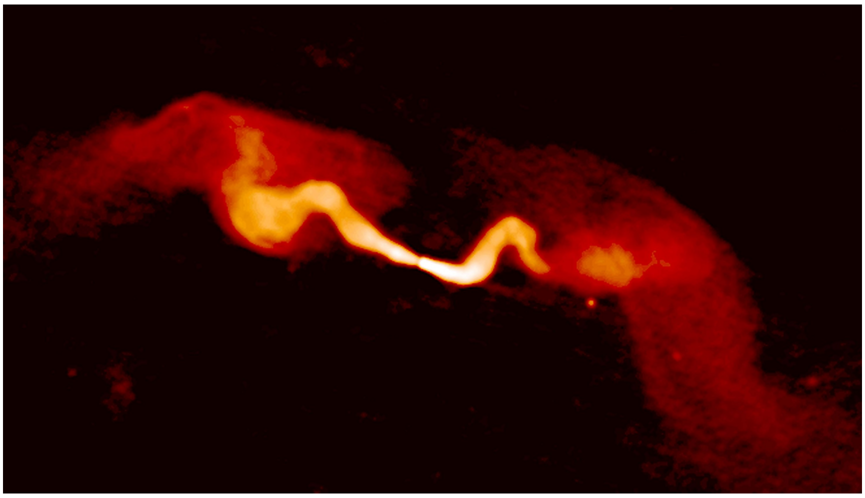

(A) Fanaroff–Riley type I source 3C 31.

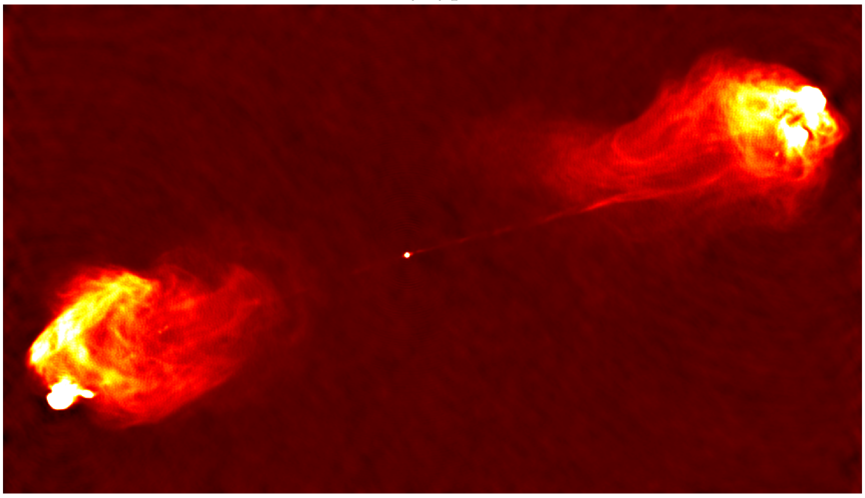

(B) Fanaroff–Riley type II source Cygnus A.

FIGURE 1.4: Radio images exhibiting Fanaroff-Riley morphologies. The 3C 31 and the Cygnus A images were obtained from the NRAO archive[1].

FR–II jets keep a substantial amount of their relativistic energy from the black hole region to the lobes but lose a good amount of their electromagnetic energy near the black hole jet region (Blandford, Meier, and Readhead, 2019). This allows them to produce strong shocks and lobes with plenty of relativistic particles and strong synchrotron emission in the region. However, FR–I jets carry their electromagnetic energy beyond the black hole jets but lose most of their kinetic energy there, resulting

[1] https://www.nrao.edu/archives/

in no or weak jet shocks. Since FR–Is still contain the electromagnetic energy out in the lobes, they are able to radiate it out in the lobes as well.

Outflows from the lobes create large-scale radio morphologies detected in MHz and GHz frequencies. Intrinsic conditions, such as hydrodynamic backflows and black hole – black hole mergers, and extrinsic conditions, such as movement of the host galaxy in the cluster, shape these large-scale structures. Conditions that form these structures can vary greatly from one radio galaxy to another.

1.4 Models of X-shaped Sources

A fraction of radio galaxies have a compact core with two pairs of radio jets, one primary jet pair and one secondary jet pair or 'wings', which form an X-shaped morphology. These X-shaped Radio Galaxies (XRGs) account for 5 to 10% of observed radio galaxies (Leahy and Williams, 1984; Leahy and Parma, 1992; Yang et al., 2019). Seven of the eleven sources in the Leahy and Parma (1992) sample contain FR–II primary lobe pairs with well-defined hotspots. The wings of all known XRGs exhibit FR–I morphology. Leahy and Parma (1992), Cheung et al. (2009), and Yang et al. (2019) have found that most of the radio luminosities of XRGs lie near the FR–I and FR–II division, and Cheung et al. (2009) and Landt, Cheung, and Healey (2010) have found them to have the average luminosity of $L_{1.4GHz} \sim 10^{25}$ W Hz^{-1}.

A suggestion by Merritt and Ekers (2002) that XRGs might be sites of radio jet axis spin-flips due to black hole binary merger events gathered more attention on these exotic radio sources. Below, we extrapolate the hypothesised processes which could give rise to the peculiar morphologies.

1.4.1 Jet reorientation

Merritt and Ekers (2002) proposed that the orientation of the spin axis of a black hole changes drastically following a coalescence of black holes, even in a minor merger. They added that since accretion onto the SMBH is constrained by relativistic frame dragging to be axisymmetric with respect to the black hole, the change in direction of the jets of the black hole will be a signpost of a merger as it is believed that the jets emitted from AGNs are parallel to the black hole's spin axis and thus launch perpendicularly to the accretion disk. Therefore, Merritt and Ekers (2002) suggested that the morphology of X-shaped sources may be a result of the reorientation of the jet due to a recent SMBH merger. In this model, the current lobe pair represents the currently active jets, while the wings represent the former jet/lobe direction.
This method of formation of X-shaped morphologies fails to explain sources which seem to have the secondary pair of jets emerging from the lobes of the primary jet pair.

Roberts, Saripalli, and Subrahmanyan (2015) looked at 52 X-shaped sources of the 100 presented by Cheung (2007) which had corresponding VLA data. They defined 'genuine X-shaped' radio sources to be those which had the second pair of lobes seemingly emerging from the core, which would likely indicate that the formation of a secondary pair of jets is a result of black hole spin axis reorientation. Following this definition, they found that 21%, at most, of identified X-shaped sources are 'genuine' and thus have a high probability of previously having a black hole merger, which makes such candidates even rarer, considering that 5 – 10% of radio-loud sources are X-shaped.

1.4.2 Superimposed jets

Another explanation for the formation of X-shaped sources is that there is a superposition of two SMBHs residing in the nucleus of the same host galaxy – each with a pair of jets but misaligned (Lal and Rao, 2005). The results that strengthen this argument are the detection of low-surface brightness lobes having flatter spectra when compared to the high-surface brightness active lobes. A flat spectral index correlates with newer emission whereas a steep one tends to correlate to older emission.

This suggestion fails to explain the morphology of systems where their secondary jets are not lying on the same axis, such as those seen in Z-shaped galaxies. The model also does not hold water in systems where the extended wings have a steeper synchrotron spectrum, in which case other models become favourable.

1.4.3 Hydrodynamical backflow

A different proposal for the cause of the morphology that considers the source environment is the hydrodynamical backflow model. The model says that the morphologies result from more prosaic yet physics-rich fluid dynamics – a plethora of charged particles are ejected by the relativistic jets, spiralling out and accelerating due to the magnetic field at the poles of a black hole and emitting resultant synchrotron emission. As detailed in Leahy and Williams (1984), the energy injection inflates radio lobes which expand against the intra-cluster or intra-group medium. If the jet power decreases or even ceases, a backflow may result due to the jet density being much less than that of the ambient medium, which then meets a higher-density hot galactic halo and may be deflected, depending on the halo dynamics and orientation. This deflection can form a pair of 'wings' – angled away from the active jets. Figure 1.5 (a) illustrates this mechanism.

Most highly-luminous sources have a pair of linear radio jets that are inversion symmetric about their host galaxies. Leahy and Williams (1984) performed simulations of the standard jet model of radio sources and found that should the jet outflow into an ambient medium much denser than the jet, a 'cocoon' of jet material will be formed depending on the density ratio of the jet and the medium. If the jet is much less dense than the ambient medium, a large amount of the kinetic energy will be converted into thermal energy, creating a broad hotspot and inflating the cocoon. The pressure in the hotspot then re-accelerates the jet material towards the centre, thus producing a backflow. The backflow stays collimated until it reaches the source galaxy to expand laterally in a fat disc upon meeting the backflow from the opposite hotspot, in an axisymmetry situation. Leahy and Williams (1984) noted that the semimajor axis of a hot ellipsoidal gas halo of the host galaxy misaligned with the jets could deflect the backflows toward the negative pressure gradient, causing them to bend and produce the secondary jets, or 'wings', of X-shaped sources.

Figure 1.5 presents morphologies which may result from hydrodynamical backflows of the lobe plasma. The backflow X-shaped morphology is explained by Fig. 1.5

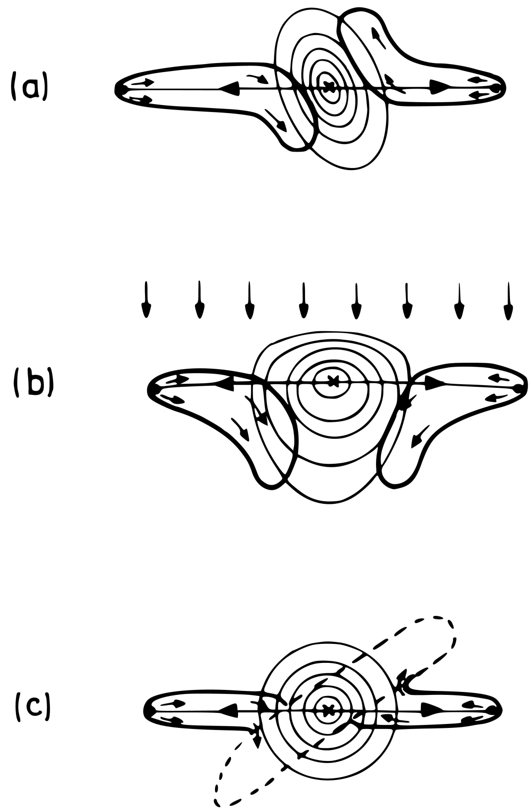

FIGURE 1.5: This is reproduced from Leahy and Williams (1984) Figure 6. Symmetry-breaking mechanism diagrams of radio jet morphologies. In each of the diagrams, the following styling represents certain information: X – radio core; thin lines – X-ray contours; and arrows showing the flow direction. The big arrows directed away from the core (X) show the direction of ejected jet material, which terminates at the dots. The small arrows from the dots represent the backflow of jet material, which meets the hot galactic halo (shown by X-ray contours), and gets deflected away (as indicated by curved arrows).

(a). In (b), we encounter a situation where, in addition to the backflow of the lobe plasma, the source galaxy is moving through the intergalactic medium in which it resides. A ram-pressure gradient is formed across the bridge of plasma emission and the gas halo of the galaxy is distorted by the galaxy's interaction with the surrounding medium. Sketch (c) presents a situation in which the source axis has varied significantly before, where the old cocoon provides a channel where the backflow from the new lobes can get deflected.

Hardcastle et al. (2019) argued for the hydrodynamical backflow model to explain the observed source morphology in the dual-AGN galaxy NGC 326.

Cotton et al. (2020) expanded on how the position angle and ellipticity of the hot gas halo, as well as geometries of the primary jet, the backflow and the semimajor axis of the hot gas halo, were key to producing the "X-shape" observed in the source PKS 2014-55. The high ellipticity of PGC 064440 (central component of the radio source) allowed the deflection of backflows without splitting them toward the most negative pressure gradient. In Figure 1.6, their total intensity map is shown.

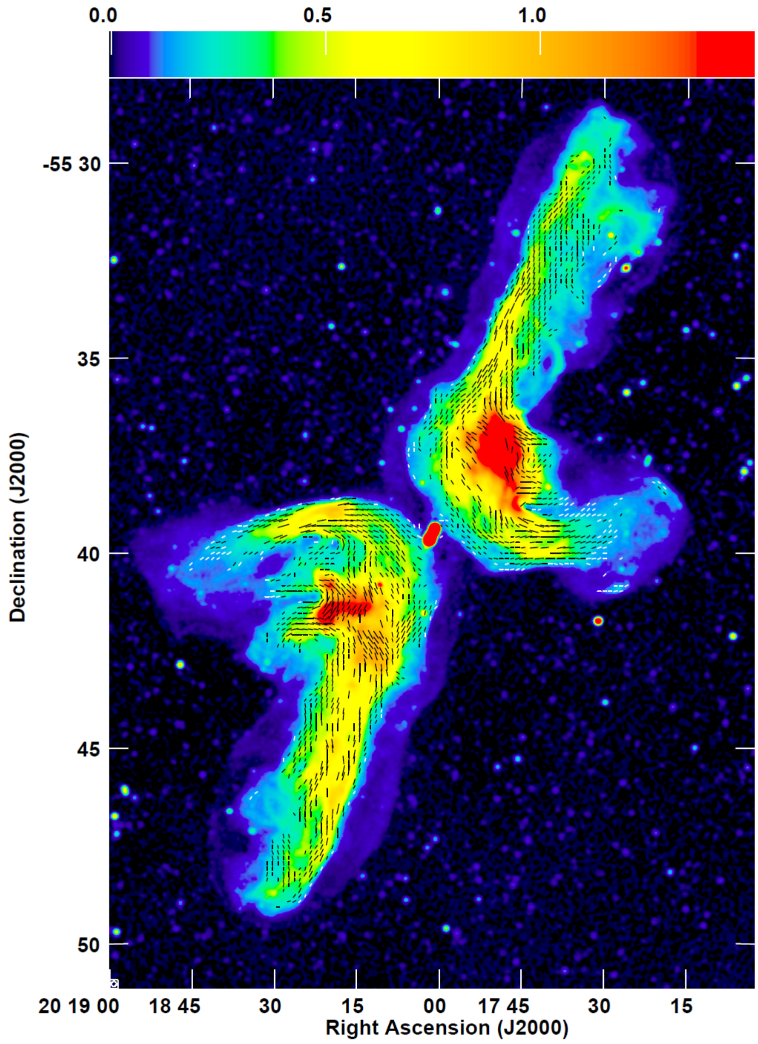

FIGURE 1.6: This is reproduced from Cotton et al. (2020) Figure 5. Total intensity colour map of PKS 2014-55, a 'double boomerang' radio source. The colour bar is linear and ranges from −0.005 to 1.5 mJy beam^{-1}. The black and white lines reveal the magnetic field lines and are of 1 arcsec length.

1.4.4 Other models

We note that there are various other models proposed for the X-shaped sources. These include situations where there was restarted nuclear activity in the host galaxy (Bruni et al., 2019); and those in which there is a slow, continuous (not sudden) reorientation of the central SMBH spin axis, which would result in the reorientation of the primary jets (Ekers et al., 1978) – strong argument for S-shaped sources as the two 'C's trace out the source history. Lalakos et al. (2022) noted that apart from the proposed models of the formation of these sources, other scenarios might exist and that the combinations of these models are plausible as well.

1.5 Introduction to NGC 326

NGC 326 is a galaxy located at $0^h58^m22.7^s$, $26°51'55''$, J2000, at a redshift $z = 0.0474$ (Werner, Worrall, and Birkinshaw, 1999). It consists of two components and we will refer to the northern one as 'core 1' and the southern one as 'core 2'. Core 1 is $\sim$ 25% brighter than core 2 (Battistini et al., 1980), with the two optical nuclei having a projected separation of 6.6 kpc (Wirth, Smarr, and Gallagher, 1982). The radio source of NGC 326 is associated with core 1. Valentijn and Casertano (1988) described NGC 326 as a 'type 1' dumbbell system, which means it has equal-magnitude components. It was Matthews, Morgan, and Schmidt (1964) who described certain multiple nuclei galaxies as 'dumbbells', whom we quote verbatim:

> *"This is a group allied to the D galaxies, in which two separated, approximately equal, nuclei are observed in a common envelope. They may well be related to the galaxies which have one or more fainter companions in their envelopes, the dumbbells being the extreme cases of very close multiple galaxies when there are only two equal components."*

The radio galaxy serves as a prototypical source for the X-shaped sources and has wings longer than its primary jets in projection – making its morphology even more peculiar. Murgia et al. (2001) found the source to have a total radio luminosity of 8.7×10^{24} W Hz^{-1} at 1.4 GHz[2]. According to the Fanaroff and Riley (1974) classification, this amount of luminosity corresponds with Fanaroff-Riley Type-I (FR–I) sources, although the value lies below the Fanaroff-Riley luminosity break, which usually has jets that are lower powered and subsonic. Murgia et al. (2001) found no hotspots in their radio images – further solidifying the suggestion that the source is of Fanaroff-Riley Type-I. The VLA observations by Murgia et al. (2001) also found the following flux values at 1.4 GHz (20 cm): south lobe – 213 mJy; north lobe – 576 mJy; east wing – 536 mJy; and west wing – 288 mJy. In this observation, the east wing was more pronounced than the west wing.

1.6 X-ray Observations

NGC 326 and its cluster atmosphere were studied in the X-rays using the *ROSAT* Position Sensitive Proportional Counter (PSPC) by Worrall, Birkinshaw, and Cameron (1995) for 21 ks. They found the X-ray atmosphere to be asymmetrical, with a full extent of $\gtrsim 800$ kpc and luminosity 3.5×10^{36} W. Close to NGC 326, the X-ray emission is mostly diffuse, with an unresolved peak coincident with the location of the radio galaxy. The temperature of the diffuse X-ray emission was found to be 1.9 keV, whose peak was suggested to be due to either cooler gas or non-thermal emission of the AGN that produces the observed radio jets. They interpreted the source morphology to be a result of buoyancy forces that bent the outer radio structure.

Hodges-Kluck and Reynolds (2012) studied the *Chandra X-ray Observatory* (CXO) exposure of NGC 326, which spanned 94.4 ks and was captured by the Advanced CCD Imaging Spectrometer (ACIS). The northern component was measured to have a temperature of $kT \sim 0.7$ keV, and a model luminosity of $L_X \approx 7.4 \times 10^{33}$ W. The southern component is fainter with no obvious nuclear point source. Its total luminosity is $L_X \sim 6 \times 10^{33}$ W. Hodges-Kluck and Reynolds (2012) confirmed the asymmetrical nature of the X-ray environment and their measured cluster temperatures agreed with those of Worrall, Birkinshaw, and Cameron (1995), detecting $kT \gtrsim 2$ keV around the core and $kT \sim 1.5$ keV near the cluster edge. They also found that the

[2] $L_\nu = 10^{24.6}\, h^{-2}$ W/Hz; $h = H_0/100$ km s^{-1}Mpc^{-1}; $H_0 = 67.8$ km s^{-1} Mpc^{-1}

X-ray peak is associated with the northern lobe of the radio galaxy. In addition, they found a high-temperature front to the southeast assumed to be a shock front, high-temperature knots of emission and an elliptical enhancement around the radio galaxy, and a cavity associated with the eastern wing.They proposed that the source was likely once an FR–II source, which has now decayed to an FR–I, due to the presence of the shock front, the size and shape of the lobes, and the GHz emission at the edges of the wings.

Hodges-Kluck and Reynolds (2012) argued for reorientation to be the cause of the observed radio source morphology of NGC 326 on the premise of wing growth speeds and the wings being longer than the active jets. However, they noted the limitation of their argument in explaining the plume on the east wing that they observed in VLA images of Murgia et al. (2001).

1.7 NGC 326 Environment

The radio galaxy NGC 326 has been found to be in the north-western quadrant of the Zwicky cluster 0056.9+2636 (Zwicky and Kowal, 1968), who then described the cluster as 'medium compact' and in the 'near' distance. Werner, Worrall, and Birkinshaw (1999) reported on their optical spectral measurements of the cluster to determine the redshifts of the constituents, and found the average heliocentric velocity of the cluster to be $c\bar{z} = 14\,307 \pm 224$ km s^{-1}, equivalent to $\bar{z} = 0.0477 \pm 0.0007$. They also reported on the one-dimensional velocity dispersion, $\sigma_z = 599^{+230}_{-107}$ km s^{-1}, which gives a three-dimensional physical velocity dispersion of $\sigma = 1\,037^{+427}_{-241}$ km s^{-1}. Other earlier measurements of NGC 326's velocity were in agreement with those of Werner, Worrall, and Birkinshaw (1999) including the X-ray measurements of Worrall, Birkinshaw, and Cameron (1995), and confirm that the X-ray emission is associated with the galaxy NGC 326.

As the X-ray atmosphere of the cluster was found to be asymmetrical, a subdivision of the cluster into the north-western and the south-eastern halves yields: (i) asymmetric gas morphology peaking in X-ray at NGC 326, in the north-western part, with a temperature of $kT = 1.9^{+0.9}_{-0.4}$ keV, suggests that the cluster segment is young (Worrall, Birkinshaw, and Cameron, 1995); and (ii) the south-eastern part is rich in galaxy count but with little hot gas and no associated velocity dispersion information.

To the south-west of NGC 326 lies the cluster Abell 115. It has an optical position of $0^{\mathrm{h}}56^{\mathrm{m}}$, $26°19'$ (J2000) and a redshift of $z = 0.1971$ (Abell, Corwin, and Olowin, 1989). The cluster is 45.8 arcmin, 778 Mpc, away from NGC 326. *Einstein Observatory* observations using the Imaging Proportional Counter (IPC) have revealed a double peak in the X-ray (Forman et al., 1981). The cluster undergoing a merger of two subclusters has a hot Intracluster medium (ICM), and cool sub-cluster cores (Forman et al., 1981; Gutierrez and Krawczynski, 2005).

1.8 Project Outline

In this project, a MeerKAT 1.28 GHz observation of NGC 326 is presented. We investigate the nature of the radio structure of the source, including its main jets, lobes and the extended wings, as well as the large-scale extension of the structure. Spectral Energy Distributions of the source are studied and presented via spectral index images of the source.

This thesis is assembled as follows: Chapter 2 covers the details of the observation of the source and the data processing that was done to produce meaningful images. All the steps that were involved in the calibration and imaging are described. The results of our investigation are then described in Chapter 3. Among the results are the MeerKAT continuum maps, determination of the spectral luminosity of the radio source, neighbouring galaxies survey, multi-wavelength data, and spectral index images. In Chapter 4, the extended discussion of all results is presented, and what they may imply about the nature of the source structure with its literature information taken into account. Chapter 5 contains the summary and conclusions of our work, and gives a discussion regarding future work.

The cosmological parameters that are used throughout the dissertation are: Hubble constant $H_0 = 67.8$ km s^{-1} Mpc^{-1}, matter density parameter $\Omega_{\text{matter}} = 0.308$ and vacuum density parameter $\Omega_{\text{vacuum}} = 0.692$ (Planck Collaboration et al., 2016); and the 3K CMB reference frame was used in correcting the redshifts where necessary. Thus, NGC 326 is at comoving distance $D_C \approx 207$ Mpc, luminosity distance $D_L \approx 217$ Mpc, and angular diameter distance $D_A \approx 198$ Mpc. That means 1 arcsec corresponds to 0.96 kpc.

Chapter 2

MeerKAT Observation and Data Processing

In this chapter, we outline the details of the radio continuum observation of our source of interest, NGC 326, and the techniques applied to process and analyse the data, thereby producing images that capture the large-scale environment in which our galaxy resides. We calibrate these radio data to correct for effects that interfere with the observed results.

2.1 Motivation for GHz observations

Radio astronomy observations performed at GHz frequencies offer a typical response to objects of scales of kpc to hundreds of kpc with sub-arcsecond (arcsec) to arcminute (arcmin) resolutions when observed by telescopes such as MeerKAT (Jonas and MeerKAT Team, 2016), VLA, e-MERLIN and ATCA. At these scales, we can study lobes, jets and hotspots of radio objects (Laing and Bridle, 2002), as well as large samples of them (Fernini et al., 1993; Hardcastle et al., 1997). Observations of the polarisation at the GHz frequencies reveal the magnetic field configurations in the jets, lobes and their hotspots (Laing, 1980).

MeerKAT GHz frequency observations provide high-fidelity imaging of extended low brightness emissions and the detection of micro-Jansky radio sources. In addition, the measurement of polarisation and the detection and monitoring of transient radio sources is afforded (Booth and Jonas, 2012).

With the presence of hundreds of MHz frequency observations corresponding to high-fidelity GHz observations of a source, detailed spectral imaging, spectral ageing (Hargrave and Ryle, 1974; Carilli et al., 1991), and broadband polarisation studies (Laing, 1988) are made possible as a result.

2.2 MeerKAT

MeerKAT is a radio interferometer which consists of 64 antennas and is located in the Northern Cape, South Africa. 48 of the 64 dishes are located in the central ~ 1 km diameter core, and the rest of the 16 dishes spread out to form an ~ 8 km maximum baseline. Each of the dishes has an offset Gregorian design and consists of a 13.5 m diameter main reflector and a 3.8 m diameter sub-reflector. The design ensures a clean optical path that is unobstructed by struts or the receiver, and in doing so, the imaging dynamic range is improved by having the primary beam sidelobe sensitivity lowered and the radio frequency interference (RFI) reside outside of the main lobe. The design also improves the dynamic range by limiting ground radiation pickup, which reduces the thermal system noise. In-depth details of the receptors of MeerKAT are discussed by Camilo et al. (2018) and Mauch et al. (2020).

2.3 Calibration and Imaging

NGC 326 was observed by MeerKAT on 11 August 2019. The observation utilised 61 of the 64 antennas, as the rest were not available due to maintenance. The observations were carried out in the L-band, and ranged in frequency from 856 MHz to 1712 MHz, for a total bandwidth of 856 MHz and a central frequency of 1.284 GHz. The longest of the 1830 baselines (for $N_{\text{antennas}} = 61$) was 8 km, while the minimum was 29 m. At the central frequency, hence, the angular resolution ranges from 6 arcsec to 27 arcmin.

The total observation time was 4.49 hours, while the time on-source for NGC 326 was 3.49 hours. A 2-second integration time was configured on the correlator for each visibility; however, this was averaged down to 8 seconds to ease the data processing requirements. The MeerKAT correlator was configured in the 4k mode, which meant that the orthogonal linearly polarised feed correlations XX, YY, XY, and YX were divided into 4096 channels, of which each has a 209 kHz width, for a total bandwidth of 856 MHz.

We performed the data reduction and processing of the MeerKAT data using the OXKAT[1] pipeline (Heywood, 2020). OXKAT is a set of scripts written in PYTHON that semi-automatically process MeerKAT data. As of writing this paper, the pipeline's default caters for full-band Stokes–I continuum imaging at L-band or UHF. The OXKAT pipeline makes use of the following software packages: Common Astronomy Software Applications (CASA[2], McMullin et al., 2007), whose purpose is to perform the averaging, flagging, splitting, and cross-calibration; SHADEMS[3], which plots the visibilities; RAGAVI[4], which plots the gain solutions; TRICOLOUR[5] (Hugo et al., 2022), which performs automated flagging, tailored to MeerKAT; WSCLEAN[6] (Offringa et al., 2014), which does both imaging and model prediction; CUBICAL[7] (Kenyon et al., 2018), which does the Direction Independent (DI)/ Direction Dependent (DD) self-calibration; and DDFACET[8] (Tasse et al., 2018), which is responsible for the imaging with direction-dependent corrections. The processing ran on the Ilifu/IDIA[9] cluster – a computing big data infrastructure for data-intensive research.

2.3.1 Flagging and calibration

Table 2.1 presents the properties of the MeerKAT observation for the target source, which includes scans of the absolute flux, bandpass, and time-variable gain calibrators. Table 2.2 shows the location of the target and calibrator sources as well as

[1] https://github.com/IanHeywood/oxkat
[2] https://casa.nrao.edu/
[3] https://github.com/ratt-ru/shadeMS/
[4] https://github.com/ratt-ru/ragavi/
[5] https://github.com/ska-sa/tricolour
[6] https://gitlab.com/aroffringa/wsclean
[7] https://github.com/ratt-ru/CubiCal
[8] https://github.com/saopicc/DDFacet
[9] https://www.ilifu.ac.za/

TABLE 2.1: Properties of the NGC 326 MeerKAT observation.

Date	11 August 2019
Number of channels	4096
Channel width	209 kHz
Integration time	2 seconds
Number of antennas	61
Image rms	17 μJy beam^{-1} (robust = -2)
Image size	10240 $\times$ 10240
Restoring beam	4.8 arcsec $\times$ 4.8 arcsec (robust = -2)
Pixel scale	1.1 arcsec
Pointing centre (J2000)	RA 0h58m24s, Dec $+26°52'0.0''$
Flux/bandpass calibrator	PKS 0408-65
Phase calibrator	J0137+3309

TABLE 2.2: Coordinates and integration time on the sources for the MeerKAT observation of NGC 326.

Name	Role	RA	Dec	On-source [h]
PKS 0408-65	Primary calibrator	04h08m20.38s	-65d45m09.1s	0.50
NGC 326	Science target	00h58m24s	+26d52m00.0s	3.49
J0137+3309	Secondary calibrator	01h37m41.29s	+33d09m35.1s	0.27

the total observation time of each. The purpose of the calibrator sources is to provide corrections to the data using known quantities or source models as a reference, since effects from the instruments themselves and those of propagation corrupt the raw data. In a process termed first-generation calibration (1GC) or cross-calibration, these corrections are applied to the target field.

The KAT Data Access Library[10] was used in converting the visibility data into Measurement Set format. In the initial inspection of the data, observational logs were viewed and bad antennas (m000, m062), as well as bad scans, were removed by flagging in the software. These flags were generated both manually and by the control and monitoring system of the telescope at the time of observation. These include antennas with abnormally large visibility amplitudes, or very low ones, those with a large offset of the phase with respect to the frequency, and those with questionable data. Following the initial flagging, offsets in antenna positions were determined and corrected. The initial 4096 channels were averaged down to 1024 channels (each channel now being 4 $\times$ 209 kHz).

Absolute flux calibration is performed on radio interferometric data to convert measured quantities into physical units. The primary calibrator, source PKS 0408-65, was used as the flux calibrator. This particular source is a point source in the 1 GHz to 25 GHz frequency range, having a strong, known and constant flux. It lies $\sim$99 deg away from the target and was observed for 10 minutes before the source of interest was observed. The same source also served for bandpass calibration, resulting in it being observed five times throughout the course of the observation, approximately once per hour. The bandpass calibration is performed to correct for an imperfect

[10] https://github.com/ska-sa/katdal

frequency transfer function caused by the receivers and downstream parts of the electronic path. Tasks GAINCAL and BANDPASS in CASA were used for this purpose. Given our particular absolute flux calibrator, PKS 0408-65, a source model with 17.066 Jy beam^{-1} flux density and a spectral index of -1.179 were assumed (Heywood et al., 2022), with 1284 MHz reference frequency. Autoflagging was then performed on residual visibilities before the next iteration.

Following the derivation of delay, absolute flux, and bandpass solutions from the primary calibrator, the amplitude and phase calibration was done using the source J0137+3309 (3C48). This is a well-known absolute flux and bandpass calibrator, and fortuitously, it is sufficiently nearby to NGC 326 ($\sim$11 deg) to be used as a gain calibrator, but not so close as to cause any noticeable artefacts that would require peeling. The solution tables were now applied to 3C48. Following this, time-variable gain solutions are derived using 3C48. These are applied to correct for effects of the atmosphere (particularly at the troposphere and ionosphere) which corrupt the phases, and antenna gains (such as the system temperature) corrupting the amplitudes. These complex gains (amplitude and phase gains) vary with time, hence the calibrator has to be close to the target ($\lesssim 10-15$ degrees), and well-sampled in time (every $15-25$ minutes). In a paper by Perley and Butler (2013), 3C48 was one of the four compact radio sources which are good primary calibrators in the observational frequency of range 1 GHz to 50 GHz. These frequency-dependent complex gains and time-variable gain solutions were derived in eight spectral bins. The applied gain solutions from the flux calibrator allowed for the scaling of gains from the amplitude and phase calibrator. Using CASA's FLUXSCALE task, a model of the intrinsic spectral shape of the amplitude and phase calibrator was determined.

Following the gain and amplitude and phase calibration steps, the gain solutions are applied to the target source and split out into a separate Measurement Set. Using the TRICOLOUR package, further flagging was performed.

The MeerKAT telescope's response to the amplitude and phase with respect to the *uv* distance of the phase calibrator J0137+3309 (3C48), which is close to the target source ($\sim$ 11 deg), is presented in Figures 2.1 and 2.2. Fig. 2.2 presents the phase scatter at 8 second, 836 kHz resolution. The spread is approximately the same across *uv* distances. The amplitude and phase bandpass solutions for all the antennas used are shown in Figure 2.3

2.3.2 Direction-independent self-calibration (2GC)

Second-generation calibration follows from the first, where the target field itself is used to refine the antenna-based gain corrections, in a process known as self-calibration. Using CUBICAL, we derived the initial notion of the sky model to calibrate the data. Then, using the target field itself, correcting gains are derived. The derived gain solutions are applied to the sky model, and the process is repeated in an iterative manner. This then allows the generation of multi-frequency synthesis (MFS) images of the target field with the use of the WSCLEAN (Offringa et al., 2014) imaging and deconvolution software package. The weighting scheme we used is *Briggs* (Briggs, 1995), with a ROBUST value of -2.0. This is effectively uniform weighting, and we chose it to achieve the best possible angular resolution with the data, while trading off a higher image rms for lower sidelobes, and artefacts associated with the bright extended sources in the field. This decision was made after extensive testing with a range of ROBUST values. We chose to enforce a circular beam, with a beam width of $\sim 4.8''$. The creation of a deconvolution mask is the start of 2GC, where a blind image is formed from the data after a certain stopping criterion is reached – after either of the following is reached first: 80 000 iterations of cleaning, or when the peak residual reaches 100 μJy beam^{-1}. This derived clean mask is defined with the knowledge of it excluding regions with a local threshold of 6σ, with σ defined as the local pixel standard deviation. The image formed blindly is discarded, and its mask is kept for re-imaging purposes, repeating the previous imaging step, but with the mask now applied to generate first model image. We then generate our first model image, using this mask and cleaning to the same depth. This initial model is then used for phase-only self-calibration, allowing for the delay terms to be solved for as well. Phase-only delay calibration solutions are derived in 2 second intervals.

A visibility model is then predicted using the mask from the multi-frequency clean components. The frequency-independent phase correction solutions are applied on-the-fly, with phase and amplitude solutions derived for every 64 seconds. WS-CLEAN was now used for re-imaging of the data following self-calibration, using a lower threshold of 20μJy beam^{-1} and 680 000 iterations of cleaning. The number of w-layers were increased by a factor of 3, and multi-scale imaging was performed on scales of 0, 1, 2, 3, 4, 5, 6, 9, 12, 18, and 27. Smooth spectra were enforced during cleaning by spectral fitting a 4th-order polynomial. The final continuum image has 10240×10240 pixels, with the pixel increment being 1.1 arcsec, giving us an image extent of 3.13×3.13 deg^2, and an rms of 17μJy beam^{-1}. There are clear direction-dependent effects present for off-axis sources; however, our target of interest has relatively high image fidelity, given the complexity of the source structure and high declination for MeerKAT. We attempted peeling the bright, extended south-western source, as well as others, before solving for direction-dependent gains. Despite several employed strategies and improvements in the off-axis source artefacts, in the end, we chose to perform our scientific analysis on the 2GC image. The primary reason for this is the significant unmodelled flux suppression seen in the 3GC-calibrated images. Since our primary science is more focused on accurate spectral index analysis together with the VLA and LOFAR maps, we prioritise this over imaging fidelity.

We summarise the self-calibration processes as follows:

- Cross-calibration was performed in the 1GC stage, where RFI, bad antennas and bad scans were flagged. Complex gain solutions are applied to the target source.
- A ‘blind’ clean 10k $\times$ 10k image was formed.
- A mask is derived from this image, which excludes regions of a threshold of 6σ.
- A 10k $\times$ 10k initial model image is generated using the blind clean mask.
- Delay and phase-only self-calibration is carried out.
- Another 10k $\times$ 10k image is formed from the corrected data and mask.
- Amplitude and phase self-calibration is then performed with multi-scale deconvolution and 3 $\times$ w-layers.

- A final 10k × 10k image is produced.

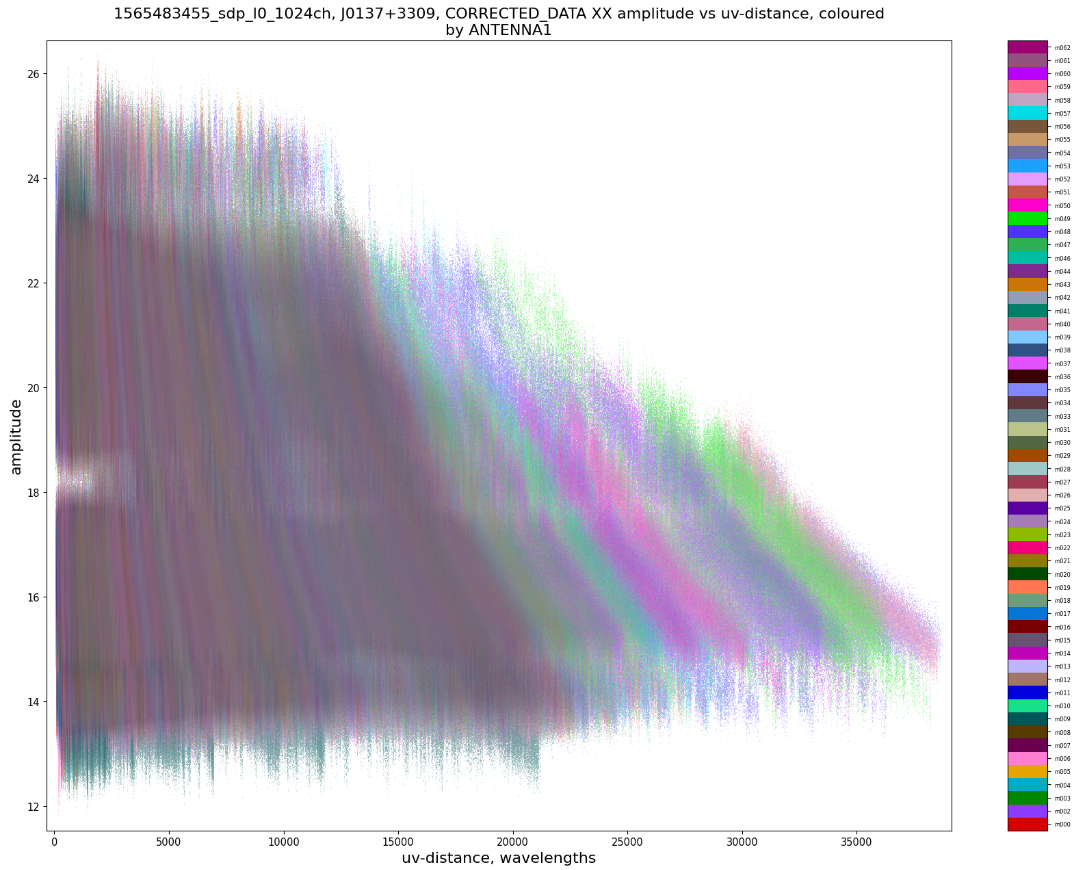

FIGURE 2.1: Visibility amplitudes with respect to the uv-distance plot for phase calibrator J0137+3309 (3C48), in the XX-correlation, during the NGC 326 observation.

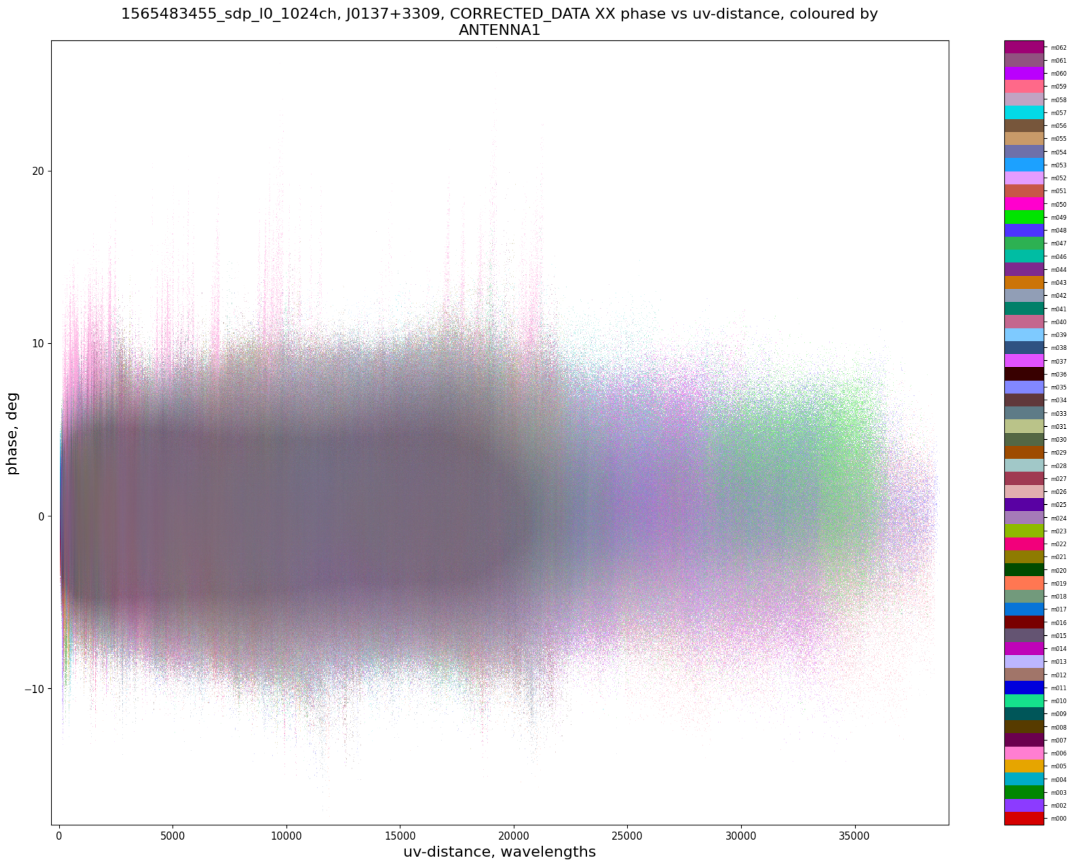

FIGURE 2.2: The response of the phase with respect to the *uv*-distance plot for phase calibrator J0137+3309 (3C48), in the XX-correlation, during the NGC 326 observation.

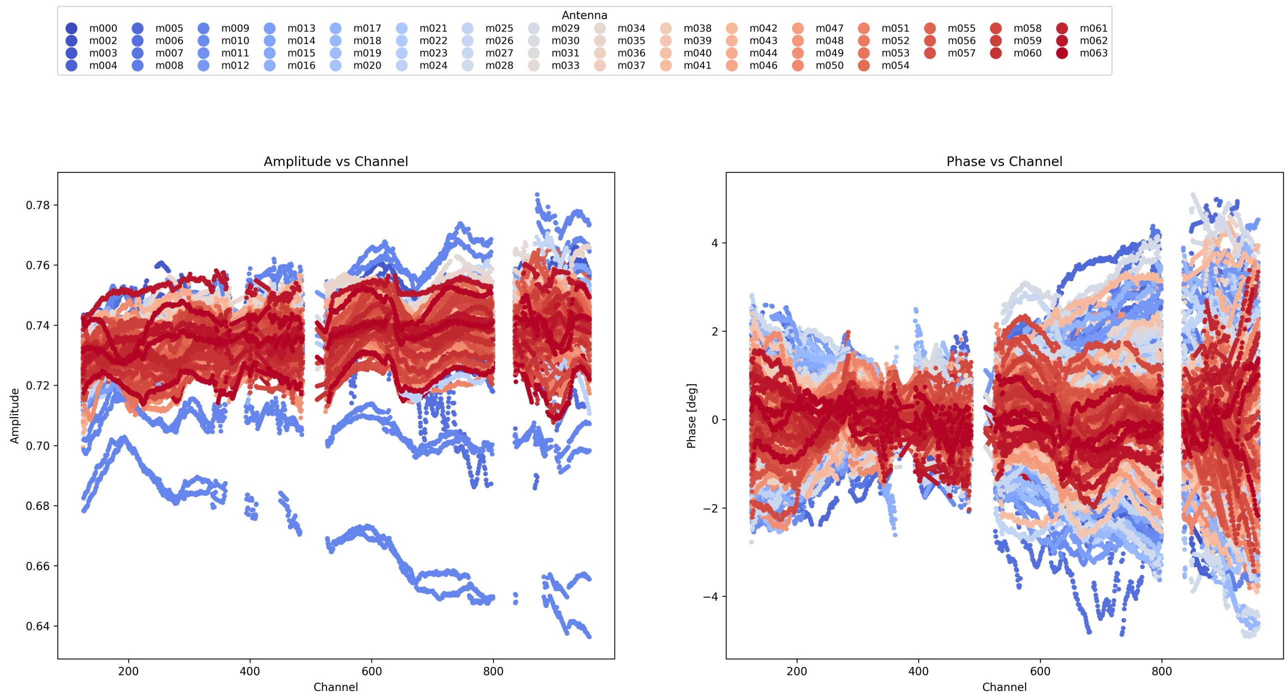

FIGURE 2.3: Amplitude and phase bandpass solutions for all antennas.

Chapter 3

Results

The results of our observations are presented in this chapter. The primary results of this thesis are the MeerKAT continuum map, the MeerKAT in-band and the MeerKAT–LOFAR spectral index results. In addition, the results presented include the commentary of the preceding multi-band radio data in contrast with ours, as well as optical and X-ray data.

3.1 MeerKAT Continuum maps

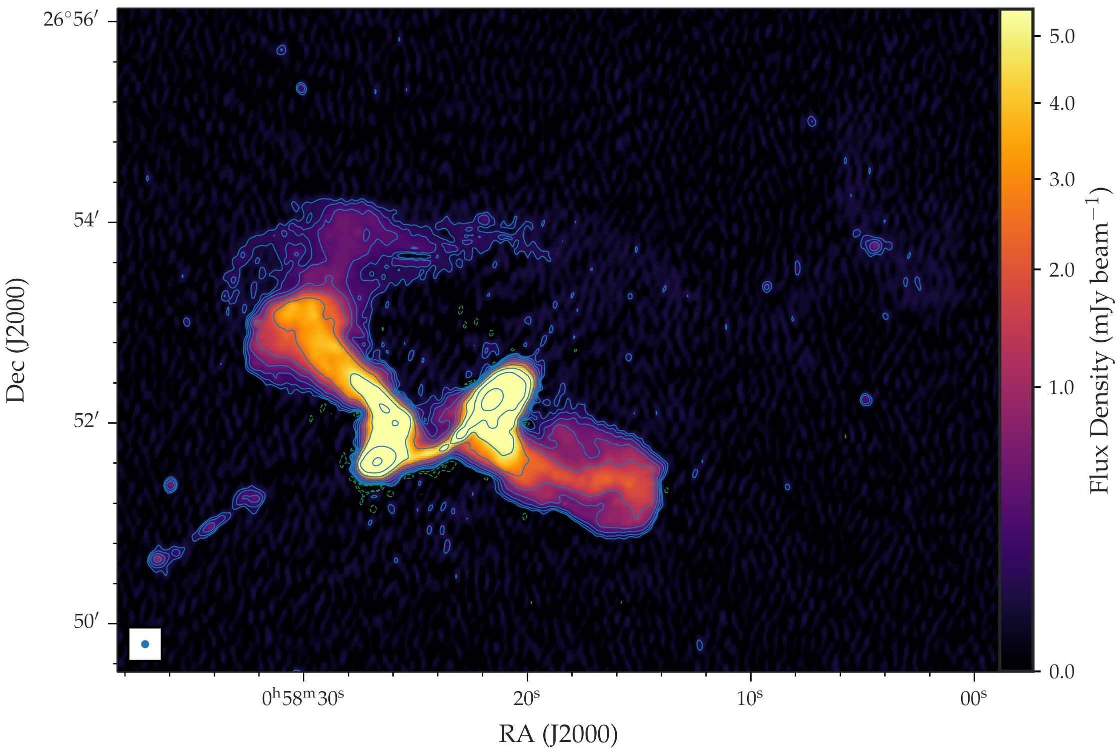

FIGURE 3.1: MeerKAT 1.28 GHz map of NGC 326. The $\theta \approx 4.8''$ Full Width at Half Maximum (FWHM) restoring beam circle is shown in the bottom-left. The colour scale of the stretch uses a square root function. With the rms noise being $\sigma = 19$ μJy beam^{-1}, the positive contours are drawn at levels $4\sigma \times 2^0, 2^1, .., 2^8$ in blue. The negative contours are drawn at levels $4\sigma \times -2^1, -2^0$ and are green.

3.1.1 The dominant X-shaped emission

MeerKAT observed NGC 326 in the L-band and we produced a 3.13 × 3.13 $\deg^2$ map of the field centred on NGC 326. Figure 3.1 presents MeerKAT's first view of NGC 326 at a resolution of 4.8 arcsec. The colour scale of the contrast used in the image is of a square root function.

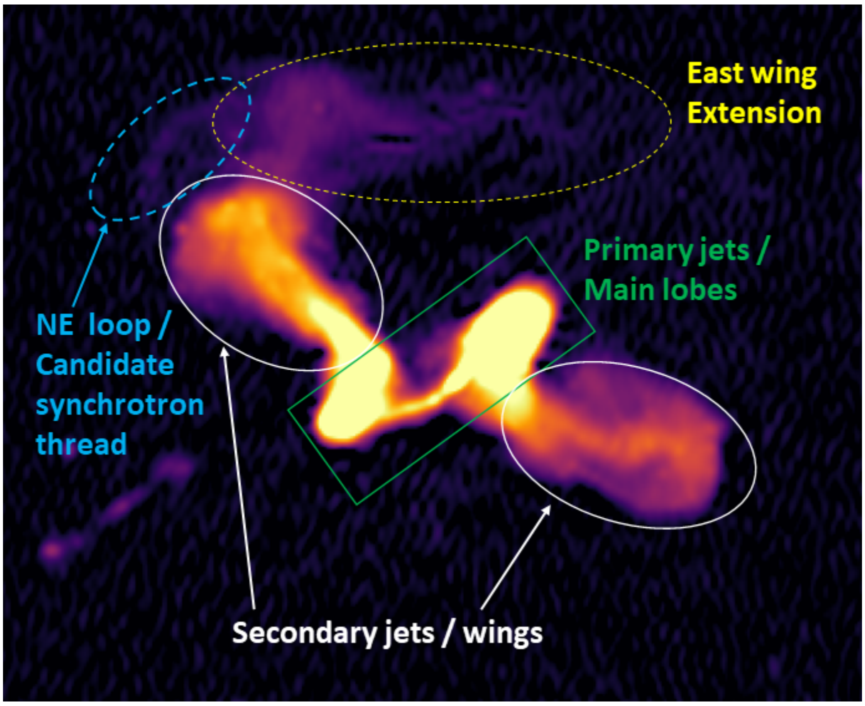

FIGURE 3.2: NGC 326 1.28 GHz map labeling different regions of the source. The labels used in the image are also used in the text when discussing the source.

The labels for different regions across the continuum source that we use in the remainder of this thesis are shown in Fig. 3.2. The exotic central 'X-shape' of the source seen in previous observations by Murgia et al. (2001) and Hardcastle et al. (2019) is plainly visible. The main jets and wings arguably form more of a 'Z' morphology, but we shall refer to the overall morphology as 'X-shaped' in this thesis for consistency with the literature. The active (primary) jets, which have large lobes, are shorter in length compared to the older and fainter wings. The primary jets exhibit an FR–I morphology – having no clear hotspots in the bright lobes, which have integrated flux densities of ~ 0.25 Jy (eastern lobe) and ~ 0.53 Jy (western lobe).

Due to the FWHM restoring beam of 4.8 arcsec, the inner structure, around the nuclei, is not resolved in these data; therefore, we refrain from commenting on the structural aspects of the core. Archival VLA data at GHz frequencies of the same source (Murgia et al., 2001) also did not have sufficient resolution to image the conditions in the nuclei, such as the black hole jets akin to those presented in Fig. 1.3, other than to confirm that both nuclei are radio sources.

The secondary jets / 'wings', are fainter compared to the main jets. The east wing and the west wing do not appear to lie on the same jet axis in projection. Moreover, the wings seem to stem from near the ends of the lobes of the primary jets. They are much longer in extent compared to the primary jets. The emission in the east wing appears to decrease smoothly when traced from the east lobe, where it appears to stem from, towards the north. This is potentially a signpost towards the radiation history and the gas dynamics in the wing. The emission in the west wing, however, drops sharply from the lobes towards the edge of the wing. In addition, the east wing is slightly more collimated than the west wing, and the brightness levels are similar at each cross-section. In the west wing, a collimated region of relatively brighter plasma connects to the west lobe and the wing edge appears to be encased in the broader and fainter plasma. The bright plasma in the west wing appears to spread out and, now being faint, flows back around the wing itself (in projection).

3.1.2 The extended diffuse emission

A large-scale extension of the east wing is observed for the first time beyond 150 MHz. In the VLA data (Murgia et al., 2001), hints of a short, faint east wing extension were visible in the 1.4 GHz A+C array configuration image (Figure 3.10). This large-scale extension was dramatically revealed with LOFAR with its 144 MHz observation (Figure 3.7) of the same source. With the current direction-independent calibration and imaging strategy, the MeerKAT map is dynamic-range–limited. A large-scale tail emission similar to that observed in the east wing is not seen in the west wing.

To the north-east of the east wing, a filamentary feature is identified (the NE loop in Fig. 3.2). The filamentary feature is difficult to identify in the LOFAR map, but is clear in the MeerKAT image. The filament appears separated from the wing edge and forms an arc, with its ends connected to the brighter and fainter edges of the east wing. It is unclear how it could have been formed. It is remarkable that MeerKAT captured the large-scale structure at its gigahertz observation, despite the low surface brightness and steep spectral index of the older plasma such as that of our source. This is attributed to MeerKAT having high imaging fidelity, sensitivity, and dynamic range (Mauch et al., 2020). For the same reasons regarding synchrotron radiation and the respective frequency, the large-scale extended tail structure is fainter in our observation compared to the LOFAR 144 MHz observation of the same source.

3.1.3 Physical properties

The luminosity distance, D_L, of the source is estimated to be 217 Mpc using the cosmological parameters stated in section 1.8. We calculate the spectral luminosity, L_ν, of the various regions of the source from its flux density, S_ν,

$$L_\nu = 4\pi\, D_L^2\, S_\nu \quad [\mathrm{W\,Hz^{-1}}]. \tag{3.1}$$

The flux density, spectral luminosity, and spectral index values are outlined in Table 3.1. The 178 MHz frequency luminosities were obtained by the spectral index formula and using the spectral index values $\alpha_{144MHz}^{1.28GHz}$. Given a frequency, ν and a flux density S_ν, the spectral index α is defined from the relationship

$$S_\nu \propto \nu^\alpha \tag{3.2}$$

as

$$\alpha(\nu) = \frac{\partial \log S_\nu}{\partial \log \nu}. \tag{3.3}$$

Since the spectral energy distributions of radio sources generally decrease with increasing frequency, we will refer to the spectral index α using the positive convention, and modify the relationship appropriately, $S \propto \nu^{-\alpha}$. Thus, the flux scaling is performed using:

$$\log\left(\frac{S_2}{S_1}\right) = -\alpha \log\left(\frac{\nu_2}{\nu_1}\right),$$

$$S_2 = S_1 \left(\frac{\nu_2}{\nu_1}\right)^{-\alpha}. \tag{3.4}$$

Details of these spectral index values are outlined in section 3.5.2. The regions surrounding the source were drawn at the 5σ-level, $\sigma = 19.3\mu$Jy beam^{-1}, and are shown in Figure 3.3.

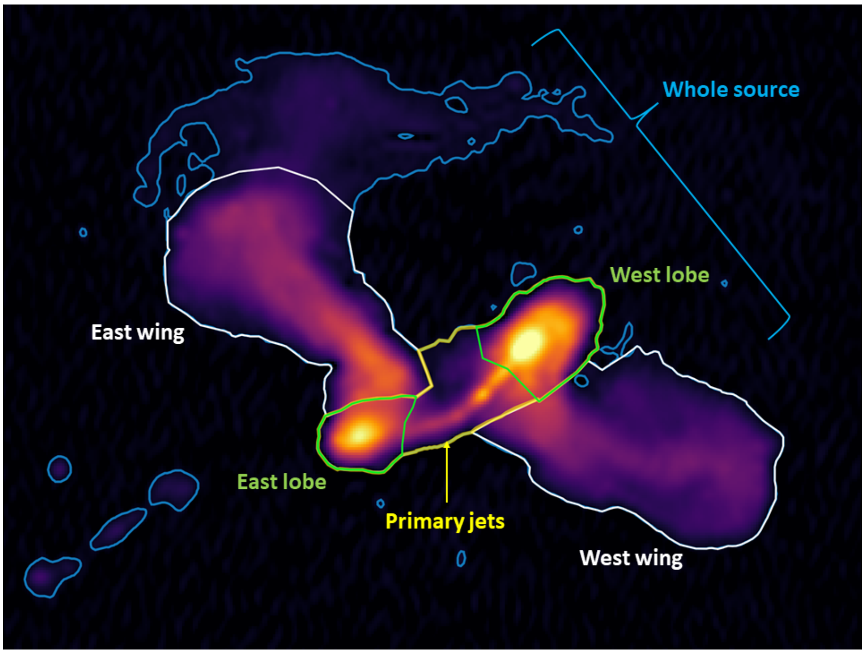

FIGURE 3.3: Regions drawn on NGC 326 at the 5σ-level from which flux densities were obtained.

We find that the total radio luminosity of NGC 326 is 1.0×10^{25} W Hz^{-1} at 1.28 GHz, which compares well with that found by Murgia et al. (2001) – 8.7×10^{24} W Hz^{-1} at 1.4 GHz[1]. Note that the radio maps presented by Murgia et al. (2001) were not as extended as ours; thus, for the radio luminosities to be comparable shows how faint the wing extensions are. The luminosity of the primary jets and lobes combined, when scaled to the frequency of 178 MHz, is 2.82×10^{25} W Hz^{-1}. This luminosity value places the source below the Fanaroff-Riley luminosity break (Fanaroff and Riley, 1974) of $\sim 2.5 \times 10^{26}$ W Hz^{-1}[2]. The ratio of the (linear) distance between the highest brightness regions on opposite sides of the central galaxy on the primary jet (1.30 arcmin) to the total extent of the primary jet measured from the lowest contour (2.23 arcmin) is 0.58, which makes the primary jets part of FR–II's (the cutoff being 0.5), on the premise of classing the object based on said ratio as Fanaroff and Riley (1974) did.

[1] $L_\nu = 10^{24.6}\, h^{-2}$ W Hz^{-1}; $h = H_0/100$ km s^{-1}Mpc^{-1}; $H_0 = 67.8$ km s^{-1} Mpc^{-1}

[2] $P_{178} = 2 \times 10^{25}$ W Hz^{-1} sr^{-1} $\times$ 4π sr (Fanaroff and Riley, 1974; Leahy, 1997)

TABLE 3.1: Flux and luminosity properties of NGC 326 at a luminosity distance of 217 Mpc, an observing frequency of 1.28 GHz, and re-scaled frequency of 178 MHz.

Region	S_ν	$L_{1.28\,\mathrm{GHz}}$	$\alpha^{1.28\,\mathrm{GHz}}_{144\,\mathrm{MHz}}$	$L_{178\,\mathrm{MHz}}$
	Jy	W Hz^{-1}		W Hz^{-1}
Whole source	1.79	1.01×10^{25}	0.983	6.28×10^{25}
Primary jets				
(including lobes)	0.940	5.31×10^{24}	0.845	2.82×10^{25}
East wing	0.530	3.00×10^{24}	0.966	2.02×10^{25}
West wing	0.277	1.57×10^{24}	1.04	1.22×10^{25}
East lobe	0.248	1.40×10^{24}	0.708	5.67×10^{24}
West lobe	0.527	2.98×10^{24}	0.814	1.49×10^{25}

3.2 MeerKAT primary beam view

Figures 3.4a and 3.4b present images with approximate dimensions of the primary beam FWHM at 1.28 GHz, $\theta = 68'$, of the observation with the target source, NGC 326, at the centre. In Fig. 3.4a, the maximum displayed flux density is set to 1.37 mJy beam^{-1} in order to show moderately bright sources. At the observing frequency of 1.28 GHz, NGC 326 is the brightest radio source in the field and is the largest in angular extent due to its large wings. Most bright sources reside within a radius of 45 arcmin from our target source. A few of them have X-ray detections, as reported by Worrall, Birkinshaw, and Cameron (1995).

Figure 3.4b displays the fainter emission in the field, where the colour-scale maximum is set to 40 μJy beam^{-1}. This is meant to show the richness of the environment in which NGC 326 resides. Spikes emerge from the off-axis bright point sources (visually similar to diffraction spikes in optical and infrared images) in Fig. 3.4b – a result of imaging artefacts and 2GC calibration limitations. Noticeably, the spikes are larger for sources farther from the centre. However, some of the extended emission is real and reveals different morphologies of the radio sources. An interesting source appears in the south-west $\sim$ 45 arcsec from the centre. It has a peak flux of 47.2 mJy beam^{-1} in our observation. The region of bright radio emission is occupied by 3C 28 – a bright FR–I source, at $z = 0.1971$ (Abell, Corwin, and Olowin, 1989), more luminous than expected for its class (Macklin, 1983), and the brightest member of the northern subcluster of Abell 115 (Forman, Jones, and Tucker, 1984; Forman et al., 2010). The same region includes X-ray sources CXOGSG J005550.4+262437 (Wang et al., 2016), 2XMM J005550.1+262436 and 2CXO J005550.3+262435. Since the south-western bright and resolved source is very near the first primary beam null, it has posed a significant challenge to calibrate it without an accurate source model and DD gain solutions.

Table 3.2 lists sources within 60 arcmin of NGC 326 extracted from NASA Extragalactic Database[3] (NED). Some of the sources are member candidates of cluster Zw 0056.9+2636 (Zwicky and Kowal, 1968). MeerKAT's maximum FWHM primary

[3] https://ned.ipac.caltech.edu/

beam is θ = 68$'$ at 1.28 GHz (Mauch et al., 2020); hence, our search for sources is of size 60 arcmin, corresponding to ∼3.46 Mpc at NGC 326's redshift. The redshift measurements in the table are spectroscopic. The heliocentric velocity of the central source NGC 326 is 14, 210 km s^{-1} and has been subtracted from the heliocentric velocities of the sources in the table, which are shown in the column ΔVelocity. Werner, Worrall, and Birkinshaw (1999) measured the redshift of NGC 326 and found a value $z = 0.0474$. The heliocentric velocities are based on the heliocentric redshift, calculated as $V = c\bar{z}$. Therefore, the positive ΔV values are farther in our line-of-sight distance, and the opposite is true for the negative values. We constrained the number of sources around the target further by choosing those with a heliocentric velocity within 2000 km s^{-1} of NGC 326, which is approximately 3.3 times the velocity dispersion of the cluster as measured by Werner, Worrall, and Birkinshaw (1999). This was done in order to include ∼ 100% of the normal distribution.

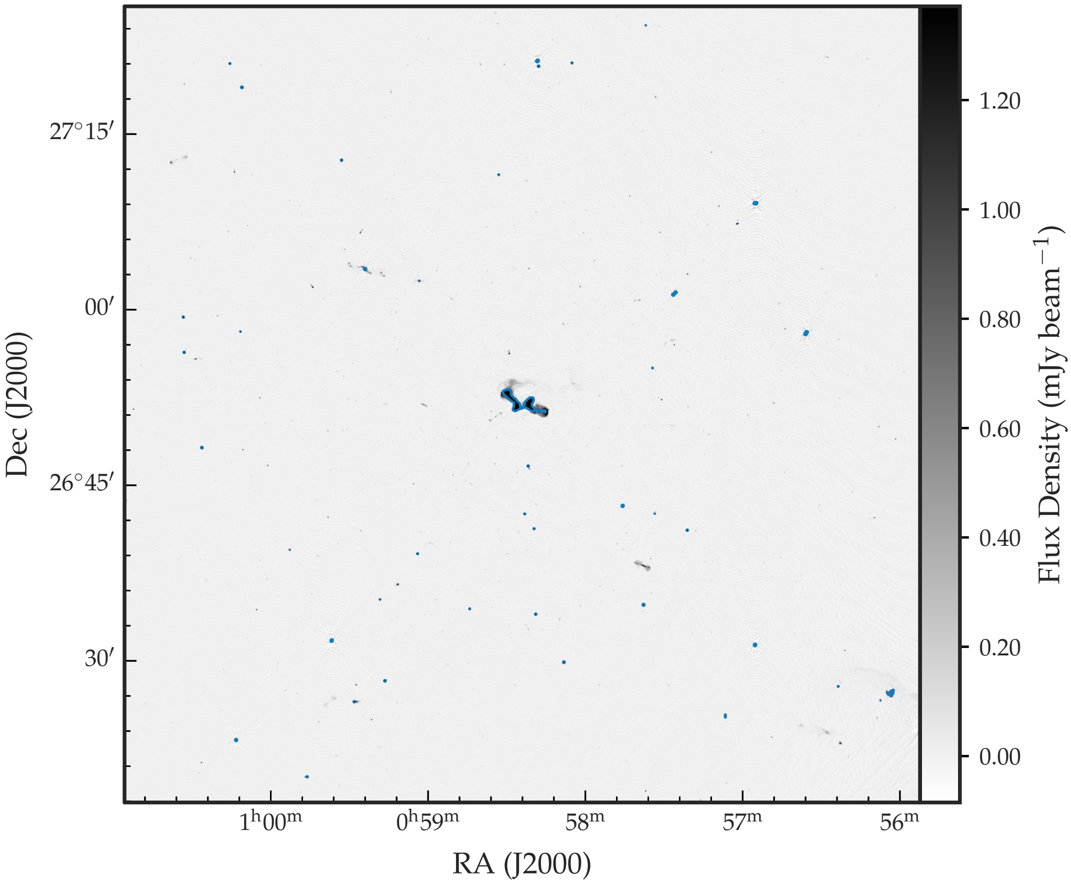

(A) Bright sources are displayed in the NGC 326 field. The colour scale is linear, with the maximum flux density set to 1.37 mJy beam^{-1}. The contours are drawn at the 1.86 mJy beam^{-1} level. The restoring beam is of size $\theta \approx 4.8''$ FWHM.

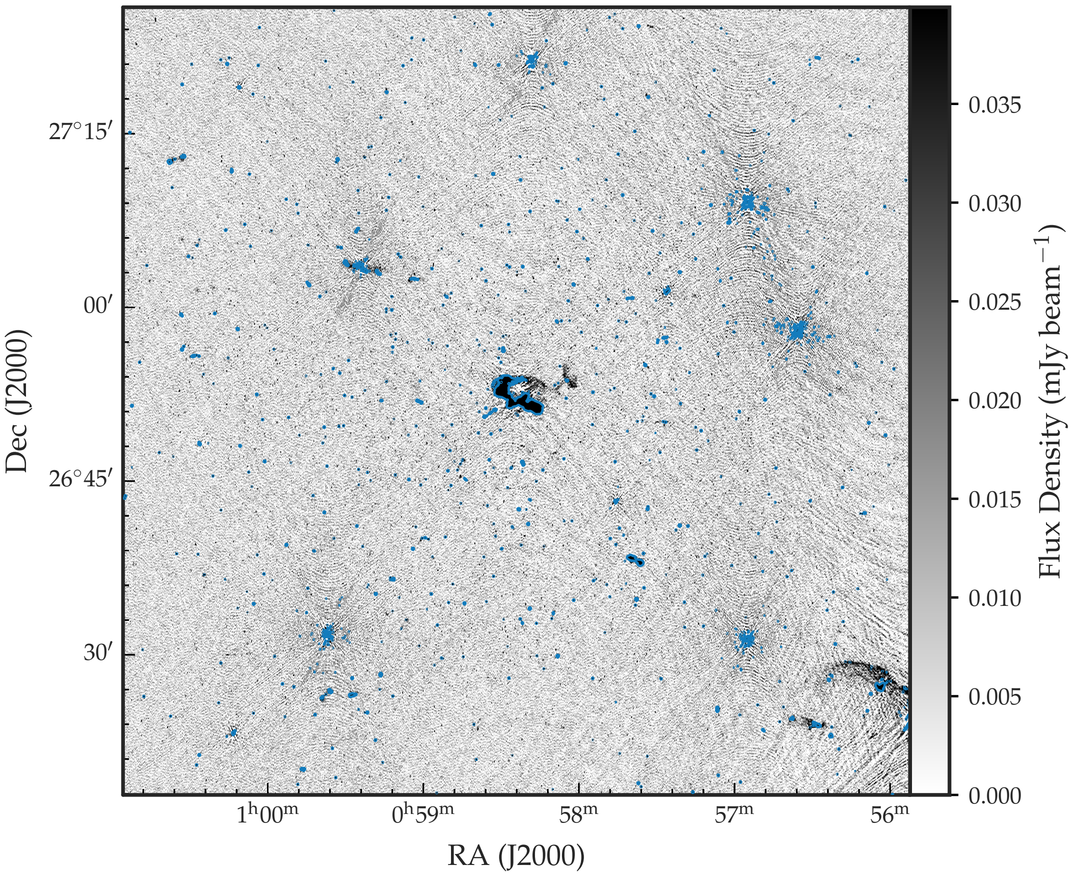

(B) Fainter sources are displayed in the NGC 326 field. The colour scale is linear, with the maximum flux density set to 40 μJy beam^{-1}. The contours are drawn at the 0.11 mJy beam^{-1} level. The restoring beam is of size $\theta \approx 4.8''$ FWHM. The lines emanating from the bright sources are artefacts resulting from the second-generation calibration.

FIGURE 3.4: The MeerKAT 1.28 GHz map of NGC 326 restricted to the size of the FWHM primary beam, $\theta = 68'$.

TABLE 3.2: Sources selected from the NASA Extragalactic Database that are within 60 arcmin of NGC 326 and within 2000 km s^{-1} of the central velocity.

Object Name	RA	Dec	Redshift z	ΔV (km s^{-1})[4]	$\Delta\theta$ (arcmin)	Separation (Mpc)
NGC 0326	00h58m22.7s	26d51m55.0s	0.0474	0.0	0.0	0.0
NGC 0326 NED02	00h58m22.8s	26d51m52.4s	0.049441	+612	0.055	9.687
NGC 0326 NED01	00h58m22.6s	26d51m58.5s	0.048734	+400	0.059	6.328
WHL J005822.6+265159	00h58m22.6s	26d51m58.7s	0.0494	+600	0.063	9.492
WISEA J005821.56+265122.2	00h58m21.6s	26d51m22.3s	0.046684	-214	0.6	3.392
WISEA J005820.25+265335.1	00h58m20.2s	26d53m35.9s	0.046062	-401	1.768	6.337
WISEA J005832.36+265148.5	00h58m32.4s	26d51m48.8s	0.047751	+105	2.159	1.67
WISEA J005828.41+265341.6	00h58m28.4s	26d53m42.0s	0.052	+1379	2.193	21.871
WISEA J005835.55+265313.1	00h58m35.5s	26d53m12.6s	0.052036	+1390	3.138	22.043
WISEA J005810.08+265026.0	00h58m10.1s	26d50m26.2s	0.047796	+119	3.178	1.888
WISEA J005816.24+264855.1	00h58m16.2s	26d48m55.4s	0.045822	-473	3.322	7.474
WISEA J005807.45+265236.5	00h58m7.5s	26d52m36.6s	0.04787	+141	3.464	2.239
UGC 00601 NOTES01	00h58m4.5s	26d53m45.6s	0.0462	-360	4.466	5.69
WISEA J005809.34+264830.9	00h58m9.3s	26d48m31.2s	0.051072	+1101	4.519	17.45
WISEA J005809.59+264759.1	00h58m9.6s	26d47m59.6s	0.0467	-210	4.893	3.33
WISEA J005841.62+265434.1	00h58m41.6s	26d54m34.1s	0.052686	+1585	4.985	25.146
WISEA J005807.01+264755.1	00h58m7.0s	26d47m55.5s	0.049287	+566	5.308	8.962
WISEA J005756.80+265617.0	00h57m56.8s	26d56m17.3s	0.052546	+1543	7.241	24.48
WISEA J005749.08+265342.3	00h57m49.1s	26d53m42.5s	0.045341	-617	7.704	9.757
WISEA J005812.30+264355.5	00h58m12.3s	26d43m55.7s	0.048357	+287	8.317	4.57
WISEA J005850.62+264558.2	00h58m50.6s	26d45m58.5s	0.05347	+1820	8.61	28.894
NGC 0326 GROUP	0h58m54.20s	26d57m2.02s	0.047	-120	8.689	1.973
GIN 026	00h58m47.4s	26d58m39.3s	0.045095	-691	8.705	10.921
RXGCC 046	0h58m51.84s	26d57m43.20s	0.0483	+270	8.711	4.304
WISEA J005749.10+265657.3	00h57m49.1s	26d56m55.3s	0.046898	-150	9.009	2.445
WISEA J005829.54+270050.0	00h58m29.5s	27d0m50.1s	0.050427	+908	9.047	14.389
WISEA J005848.13+270111.2	00h58m48.1s	27d1m11.6s	0.050845	+1033	10.872	16.382
WISEA J005916.43+265201.6	00h59m16.4s	26d52m1.7s	0.049554	+646	11.987	10.253
WISEA J005911.40+265812.2	00h59m11.4s	26d58m12.4s	0.048423	+307	12.547	4.918
WISEA J005725.28+265010.0	00h57m25.3s	26d50m10.3s	0.049704	+691	12.926	10.969
MCG +04-03-030	00h59m3.6s	27d2m32.8s	0.0486	+360	14.007	5.762
WISEA J005925.78+264800.7	00h59m25.8s	26d48m0.7s	0.049504	+631	14.6	10.031
WISEA J005929.19+265529.8	00h59m29.2s	26d55m30.1s	0.049882	+744	15.251	11.825
2MASX J00593281+2649476	00h59m32.8s	26d49m48.0s	0.046282	-335	15.778	5.386
UGCl 016	0h59m36.22s	26d52m9.88s	0.047399	0.0	16.398	1.036
2MASX J00591793+2704069	00h59m17.9s	27d4m6.7s	0.051521	+1236	17.324	19.62
WISEA J005853.79+270803.0	00h58m53.8s	27d8m3.7s	0.049704	+691	17.565	10.996
IC 0064	00h59m24.4s	27d3m32.6s	0.045932	-440	18.009	7.04
WISEA J005900.42+270846.9	00h59m0.4s	27d8m46.8s	0.048	+180	18.84	3.087
WISEA J005924.86+270720.6	00h59m24.8s	27d7m21.0s	0.047986	+176	20.732	3.075
2MASX J00594231+2639026	00h59m42.3s	26d39m2.8s	0.047183	-65	21.945	1.724
WISEA J005950.55+270303.8	00h59m50.5s	27d3m2.9s	0.052167	+1429	22.512	22.716
UGC 00585	00h56m45.4s	27d0m34.8s	0.04649	-273	23.354	4.551
2MASX J00570239+2707323	00h57m2.4s	27d7m32.0s	0.044999	-720	23.744	11.455
PPS2 089	01h0m6.3s	26d58m33.3s	0.04763	+69	24.035	1.873
MCG +04-03-021	00h56m41.9s	27d1m38.6s	0.042518	-1463	24.473	23.108
WISEA J005726.92+271313.5	00h57m26.8s	27d13m12.3s	0.053907	+1951	24.662	31.022
GIN 030	01h0m18.0s	26d56m57.8s	0.040983	-1924	26.186	30.32
CGCG 480-031	01h0m27.9s	27d1m30.8s	0.049721	+696	29.508	11.183
WISEA J010044.20+265827.1	01h0m44.2s	26d58m26.8s	0.053784	+1914	32.213	30.467
WISEA J010100.85+265815.7	01h1m0.8s	26d58m15.6s	0.046981	-125	35.818	3.003
ABELL 0115:[GDW2019] 121	00h55m56.1s	26d29m44.6s	0.047574	+52	39.54	2.637
WISEA J005523.67+271204.2	00h55m23.7s	27d12m4.2s	0.043205	-1257	44.672	20.008
CGCG 480-022	00h56m4.2s	26d18m18.9s	0.047201	-59	45.697	3.032
WISEA J010148.95+265844.3	01h1m49.0s	26d58m44.2s	0.048934	+460	46.48	7.867
WISEA J005548.96+262024.7	00h55m49.0s	26d20m25.0s	0.046944	-137	46.62	3.642

TABLE 3.2: Sources selected from the NASA Extragalactic Database that are within 60 arcmin of NGC 326 and within 2000 km s^{-1} of the central velocity (continued).

Object Name	RA	Dec	Redshift z	ΔV (km s^{-1})[4]	$\Delta\theta$ (arcmin)	Separation (Mpc)
CID 04	01h2m0.0s	26d56m60.0s	0.046999	-120	48.709	3.606
NSC J010202+265724	01h2m5.4s	26d57m6.6s	0.0488	+420	49.911	7.374
UGC 00638	01h2m5.4s	26d57m6.5s	0.048029	+189	49.914	4.357
WISEA J010115.65+272410.4	01h1m15.8s	27d24m11.6s	0.049938	+761	50.242	12.484
WISEA J010206.11+265851.0	01h2m6.1s	26d58m51.1s	0.047784	+115	50.275	3.674
WISEA J010210.81+265629.9	01h2m10.8s	26d56m29.8s	0.053166	+1729	51.059	27.649
WISEA J010211.90+264950.8	01h2m11.9s	26d49m50.8s	0.049605	+661	51.167	10.978
WISEA J010211.98+265950.2	01h2m12.0s	26d59m50.4s	0.047433	+10	51.712	3.274
WISEA J005431.13+263500.7	00h54m31.1s	26d34m60.0s	0.048577	+353	54.411	6.58
WISEA J010220.70+270721.6	01h2m20.7s	27d7m20.9s	0.04352	-1163	55.219	18.643
WISEA J010147.35+272619.3	01h1m47.4s	27d26m20.2s	0.046791	-182	57.077	4.601

[4] The heliocentric velocity difference. NGC 326 heliocentric velocity is chosen as the reference velocity; and hence, it is subtracted from the raw values to obtain the difference.

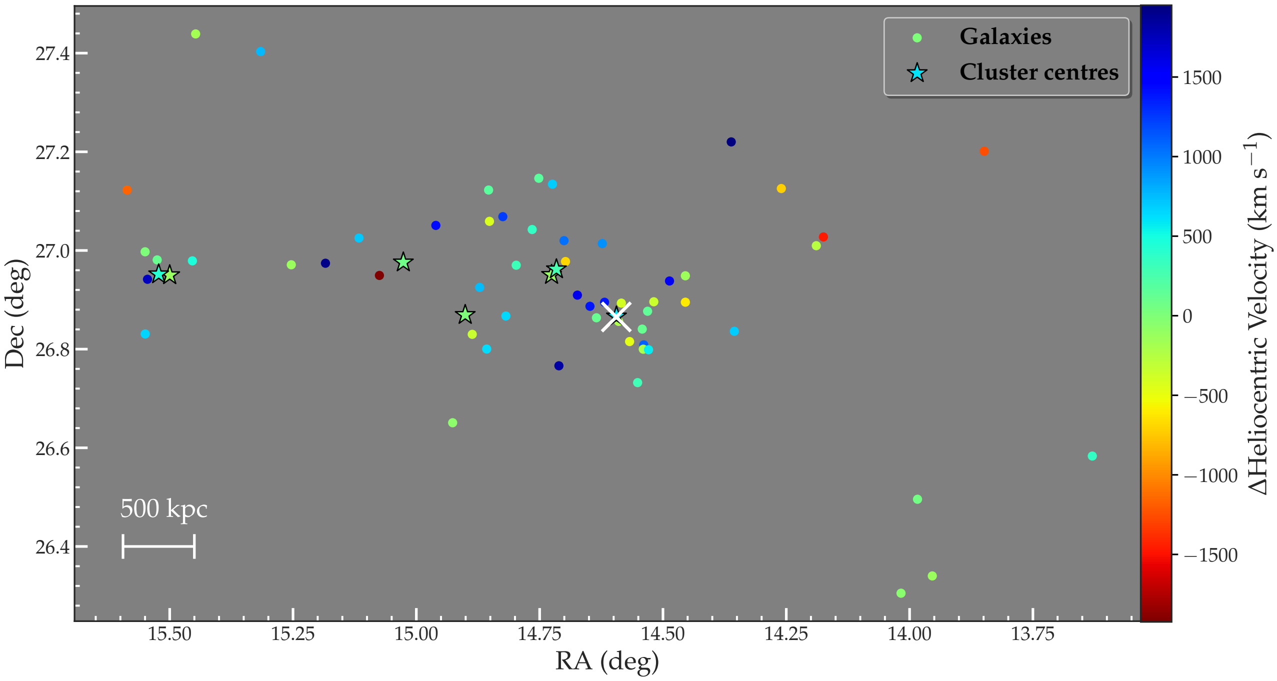

FIGURE 3.5: Scatter plot of sources within 60 arcmin of NGC 326 and 3.3σ of its cluster's velocity dispersion, centred on the redshift of NGC 326. The white cross at the centre represents the midpoint of the two cores of NGC 326. The colour of the point sources represents their respective heliocentric velocity, which has been subtracted from that of NGC 326. The star-shaped ($\star$) points represent cluster centres.

Figure 3.5 is a scatter plot of the sources presented in Table 3.2 and displayed by their location in the sky. The colours of the points represent the relative heliocentric velocity with respect to the NGC 326 system. Werner, Worrall, and Birkinshaw (1999) found that the north-western part of the cluster Zw 0056.9+2636 (Zwicky and Kowal, 1968) has velocity dispersions that are consistent with X-ray temperatures and cluster richness. Most of the sources seem to be distributed in an east-west fashion; however, it is unclear if their distribution is connected to a larger scale structure.

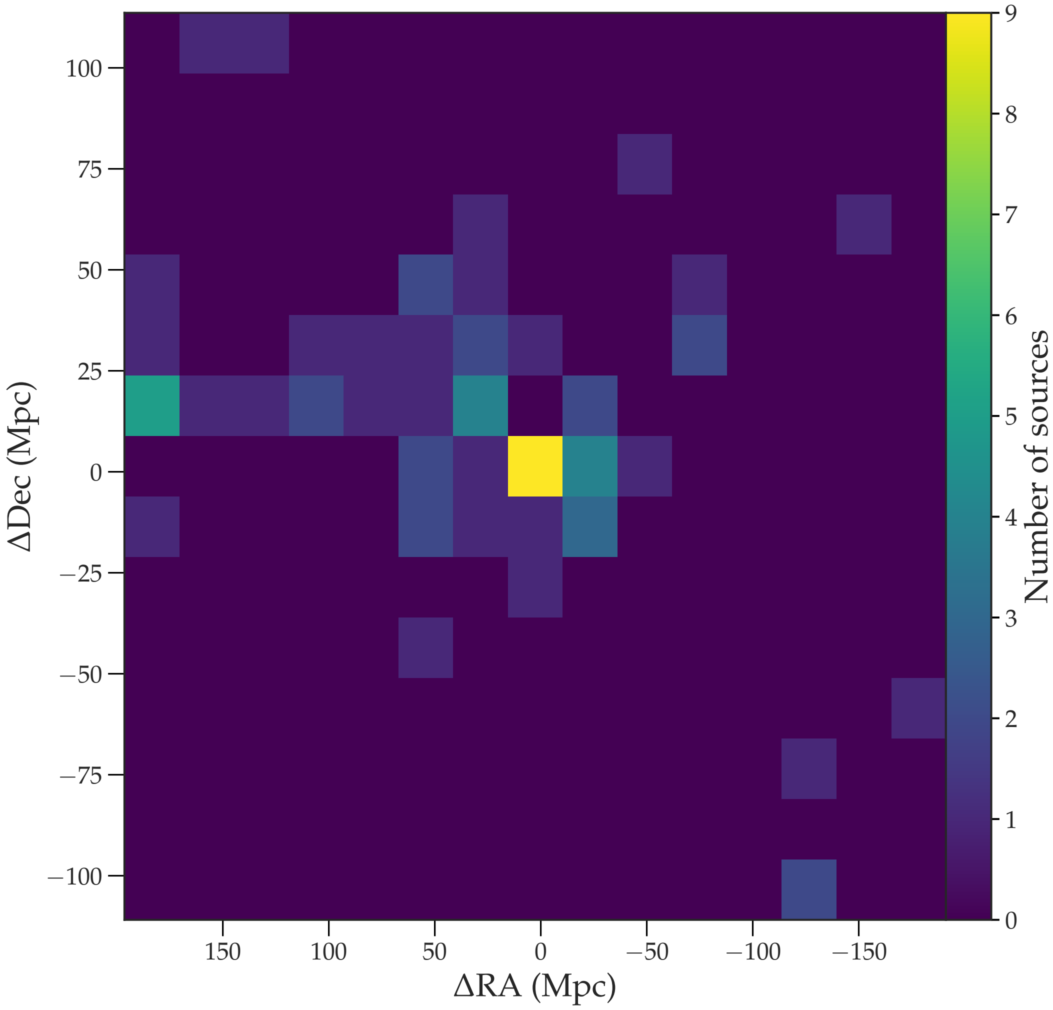

FIGURE 3.6: 2D histogram of the sources within 60 arcmin of NGC 326, represented by their separations in Right Ascension and Declination from NGC 326.

We accompany Fig. 3.5 with a 2D histogram, presented in Figure 3.6, to convey the number density of the presented sources. The sources in Table 3.2 are presented and displayed by their distance from NGC 326. The histogram demonstrates that NGC 326 is at the centre of a cluster; in addition, it shows that there is a bimodal east-west distribution of the galaxies in the field at the chosen redshift range.

3.3 Multi-band radio imaging

3.3.1 LOFAR

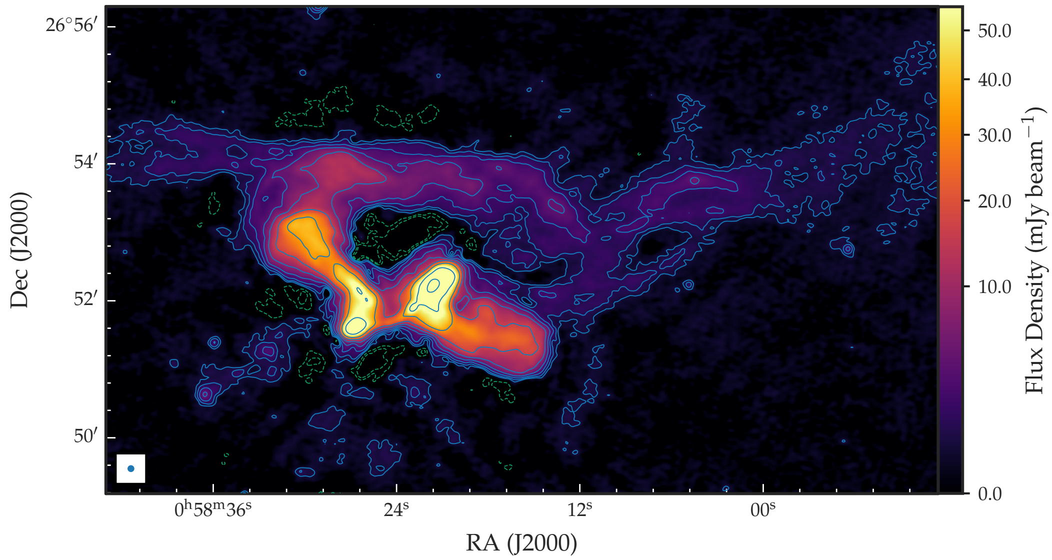

FIGURE 3.7: LOFAR 144 MHz observation of NGC 326. The colour scale of the stretch uses a square root function. The flux has been up-scaled by 1.22 following flux scale analysis with MeerKAT and VLA measurements of several bright point sources in the field. The rms noise is $\sigma = 129\mu$Jy beam^{-1}, and the positive contours are drawn at levels $5\sigma \times 2^0, 2^1, ..., 2^5$ in blue. The negative contours are green and drawn at levels $5\sigma \times -2^1, -2^0$.

LOFAR made an observation of NGC 326 as part of the LOFAR Two-meter Sky Survey (LoTSS), the results of which were published by Hardcastle et al. (2019). We obtained the mosaic of the observation from the LoTSS archive[5]. Attributed to the telescope's densely sampled uv plane coverage (having 32 stations in its compact core and 45 remote stations), 6 arcsec resolution, and the low observing frequency of 144 MHz, LOFAR was able to capture the large-scale extended 'tail' structure of the east wing that extends 13 arcmin and a filamentary tail that connects with the edge of the east wing. Hardcastle et al. (2019) argue that the extended tail structure signals the presence of coherent magnetic field enhancements, although they had no clear explanation for the bend in the tail towards the west end. Hardcastle et al. (2019) also captured a filamentary extension of the tail to the east of the beginning of the tail. In addition, the central X-shape structure visible in the VLA images of Murgia et al. (2001) is also seen at high brightness. The collimated primary jet ($S_{144}^{\rm int} \sim 1.0$ Jy), lobes (east $S_{144}^{\rm int} \sim 0.97$ Jy; west $S_{144}^{\rm int} \sim 2.3$ Jy), and wings (east $S_{144}^{\rm int} \sim 3.3$ Jy; west $S_{144}^{\rm int} \sim 2.3$ Jy) can be seen with good clarity.
As one can recall, higher-energy electrons lose energy faster to synchrotron radiation than lower-energy electrons, meaning extensions of the plasma away from the source are likely to emit radiation from the low-energy electrons; thus, LOFAR is able to capture their emission.

Upon closer inspection of the image, we noticed that the absolute flux calibration may require adjustment. Moreover, when the spectral index images were made using the LOFAR image and the MeerKAT image, the results were flatter than those

[5] https://lofar-surveys.org/

presented in the literature. Hardcastle et al. (2019) mentioned that the LOFAR flux scale is known to be uncertain, with systematic errors of order 10 per cent, as the transfer of calibration to the target field from a reference source has difficulties in it. As a result, we check for evidence of an absolute flux calibration offset. (Bonnasieux, E. et al, private communication).

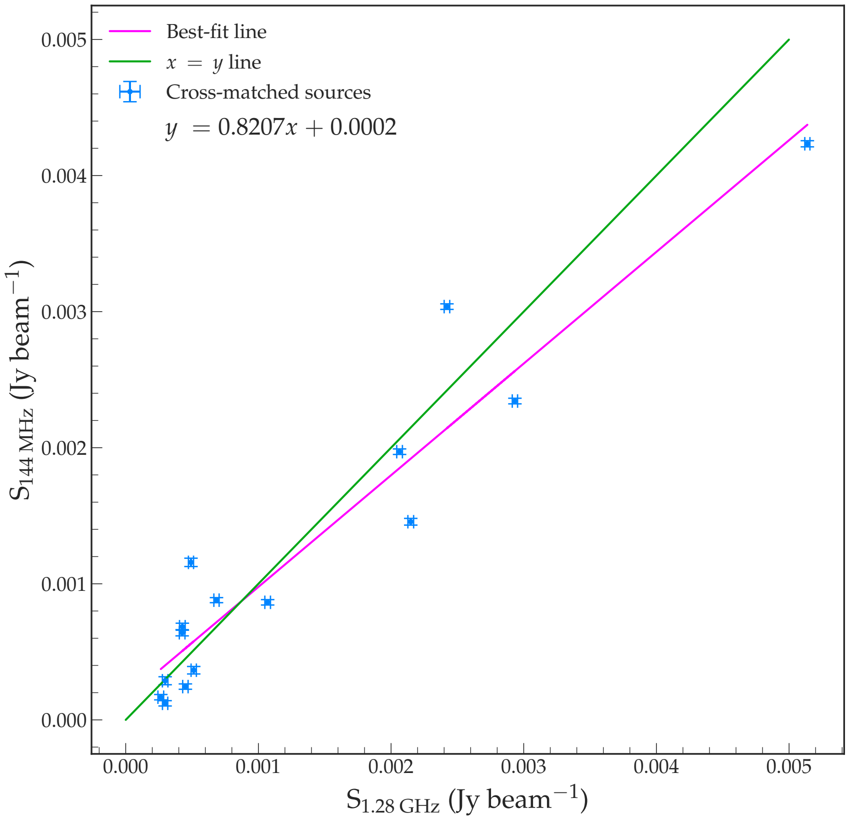

FIGURE 3.8: Manually cross-matched MeerKAT and LOFAR sources plotted against their peak Stokes–I flux densities. LOFAR flux densities have been re-scaled to the MeerKAT frequency assuming $\alpha = 0.75$. The MeerKAT data was produced with a robust parameter of zero, and the uncertainties are 1-σ error on the peak flux density per beam. The peak flux densities were chosen as they have high signal-to-noise ratios.

We used a tool called the Python Blob Detector and Source Finder (PYBDSF, Mohan and Rafferty, 2015) to extract a catalogue of bright sources present in both the MeerKAT and LOFAR images. We chose several unresolved sources within 0.5 deg of NGC 326 to minimise the impact of weighting and compared their peak Stokes I flux densities with LOFAR and MeerKAT in Figure 3.8. The LOFAR flux density values were up-scaled to the MeerKAT 1.28 GHz frequency by using the relation between the spectral index, the flux density and the observed frequency of a source (Eq. 3.4). We used the average spectral index of bright compact radio sources, $\alpha \sim 0.75$. A best-fit and a one-to-one ($x = y$) line are compared with the data. If neither the MeerKAT nor the LOFAR flux densities had an absolute flux calibration offset, the best-fit line would be, in principle, statistically consistent with the one-to-one line. This significant misalignment between the best-fit and one-to-one lines as seen in Fig. 3.8 suggests an offset in the absolute flux calibration of the two telescopes.

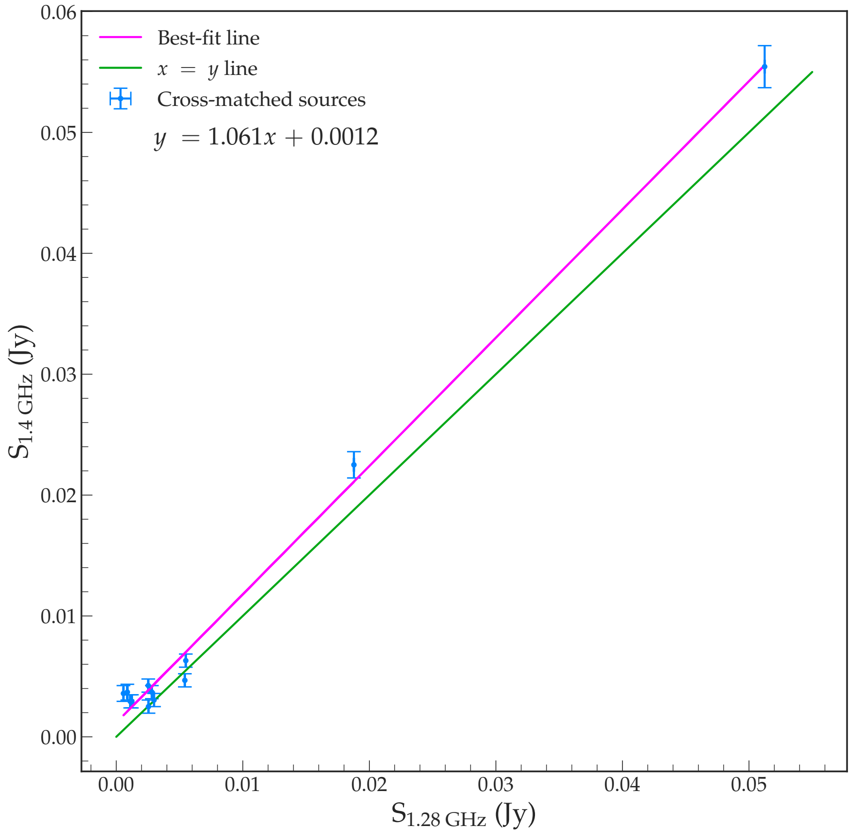

FIGURE 3.9: Manually cross-matched MeerKAT and VLA NVSS sources plotted against their total fluxes. VLA NVSS flux densities have been re-scaled to the MeerKAT frequency assuming $\alpha = 0.75$. The MeerKAT data was produced with a robust parameter of zero, and the uncertainties are 1-σ error on the total flux density.

Figure 3.9 presents a number of sources within 0.5 deg of the MeerKAT image, extracted using PYBDSF, and present in the NRAO VLA Sky Survey (NVSS) catalogue[6]. The NVSS flux densities were scaled to the MeerKAT 1.28 GHz frequency, by using Eq. 3.4 and $\alpha \sim 0.75$. The VLA is a much older, well-established telescope when compared to MeerKAT and LOFAR, meaning its absolute flux calibration systematic errors are likely lower. Therefore, the NVSS catalogue likely provides more accurate data on integrated flux densities and serves as a control in our investigation, even though it has significant differences in depth and angular resolution. From the NVSS catalogue, the reported peak fluxes for the chosen set of sources were smaller than their corresponding errors by some unknown reason. However, the total fluxes were larger than their errors, being at least 5 times greater than the associated error. The MeerKAT peak fluxes were similar to their total fluxes, with the average being

$$\overline{x} = \frac{1}{n}\Sigma_i^n \left(\frac{S_{1.28,i}^{\text{peak}}}{S_{1.28,i}^{\text{total}}} \right) \times 100\% = 90.58\%. \tag{3.5}$$

Therefore, for matching MeerKAT and NVSS sources, their total flux values were used. Since the best-fit to the data is nearly parallel to the one-to-one line, this suggests that MeerKAT and VLA have consistent absolute flux calibration, albeit with a relatively small number of sources.

[6] https://www.cv.nrao.edu/nvss/

Only three sources are present in both the LOFAR image and the NVSS catalogue within 0.5 deg of NGC 326, which are not sufficient to perform a cross-matching that would yield a sound fit to the data. However, given that the MeerKAT data is in agreement with the NVSS data, we assume that the LOFAR data has an absolute flux calibration offset. We used the gradient of the best-fit line of the MeerKAT–LOFAR plot (Fig 3.8) to correct the LOFAR flux density values and ensure a one-to-one relationship of the LOFAR flux densities to the MeerKAT flux densities. We found a value to re-scale the LOFAR fluxes as follows:

$$\text{Scale factor} = \frac{1}{\text{best-fit line slope}} = \frac{1}{0.821} = 1.22 \quad (3.6)$$

Figure 3.7 presents the LOFAR image with the above scaling factor applied.

3.3.2 NRAO VLA radio observations

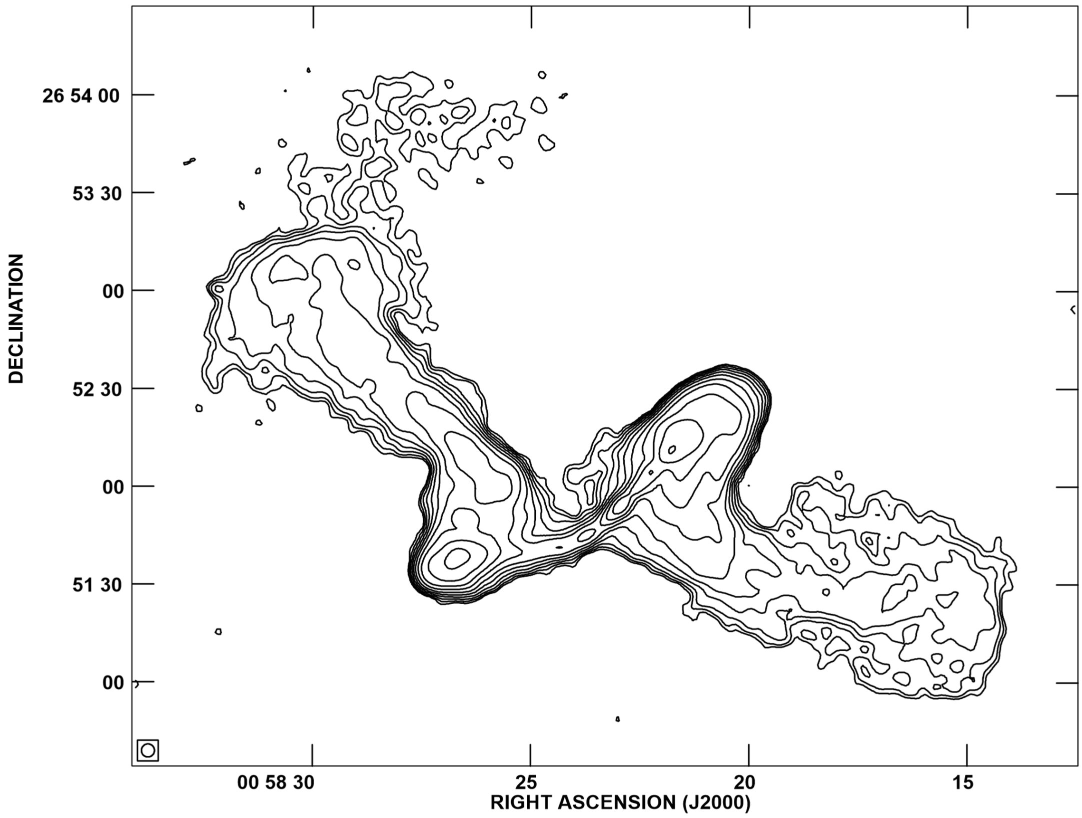

FIGURE 3.10: 1.4 GHz A+C array total intensity contour map of NGC 326 reproduced from Murgia et al. (2001) Figure 5. The restoring beam dimensions are 4″ × 4″. The contours are at levels 0.25, 0.39, 0.61, 0.96, 1.5, 2.3, 3.7, 5.7, 9, 14, 22 mJy beam^{-1}.

The VLA 1.4 GHz A+C array total intensity contours of NGC 326 shown in Fig. 3.10 are consistent with our data at a given flux density threshold. They show centre-brightened radio lobes characteristic of an FR–I type source. Additionally, the primary jet is narrow and collimated while the wings are wider and spread at the edges – results of which are consistent with the MeerKAT images presented in this work.

While the inner structure of NGC 326 is captured well in their data, the filamentary feature captured by MeerKAT and the extended wings are invisible to the VLA C-configuration L-band observations of Murgia et al. (2001) as they were sensitive to smaller scale structures of < 6 arcmin. If the VLA had the required shorter baselines and a higher sensitivity, the bright parts of the tail extension would be visible in the observations of Murgia et al. (2001). This allows us to use the VLA data for spectral index studies of primary jets, lobes and wings.

3.4 Ancillary Data

3.4.1 Hubble Space Telescope

The galaxy NGC 326 has been imaged by the *Hubble Space Telescope* (HST), which captured the galaxy's optical features. We obtained an image of the galaxy from the HST archive[7], which was taken using the HST's Planetary Camera (PC) detector and the F555W filter. Detailed analyses of the HST observation of NGC 326 and other sources were published by Capetti et al. (2000). The image had a large number of cosmic rays, which resulted in the image having very bright pixels. We removed the very bright pixels from the image and set the maximum pixel value to 2.0 counts/s. A median filter failed to work desirably as most of the pixel values were too high. This removed all the artefacts and left the outlines of the galaxy's dual nuclei visible. Figure 3.11 presents the HST image contours overlaid on the MeerKAT image of the core of NGC 326. The contour lines were then drawn at various levels to highlight the two cores, which were then overlaid onto the MeerKAT map and the spectral index maps.

[7] https://hla.stsci.edu/hlaview.html

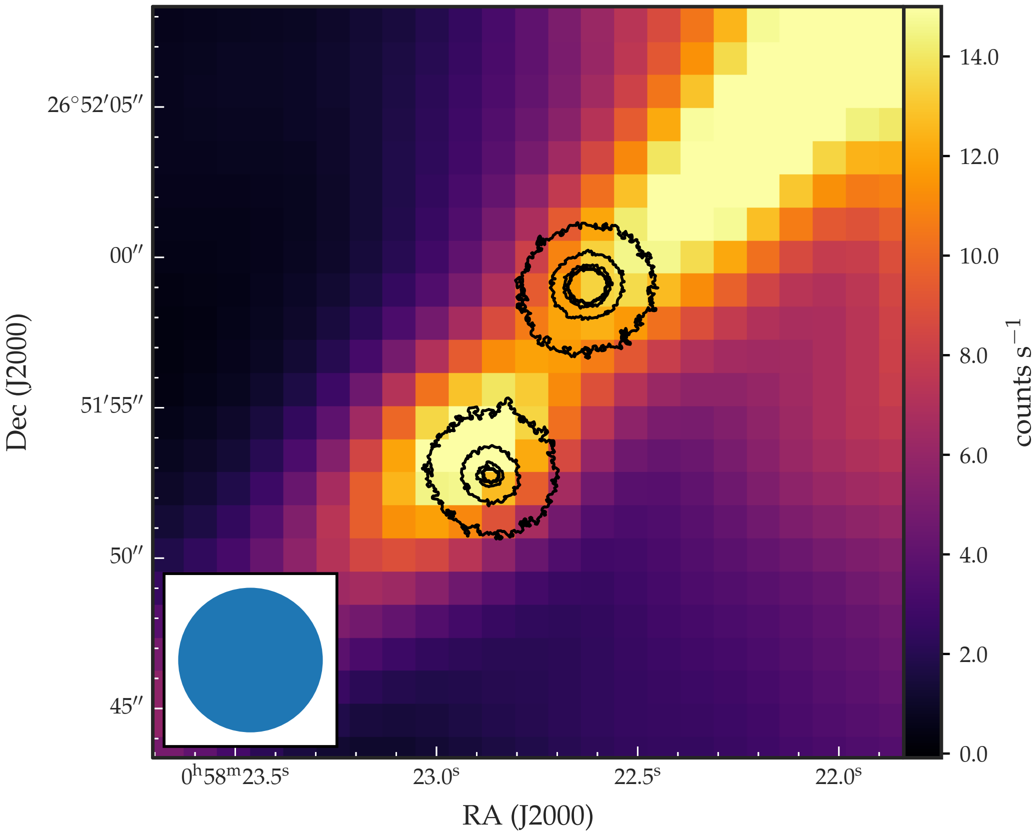

FIGURE 3.11: NGC 326 optical nuclei overlaid onto the MeerKAT 1.28 GHz map. With the rms noise being $\sigma = 0.0910$ counts s^{-1}, the contours were drawn at the levels $\sigma \times 2$, 5 and 9. The 4.8 arcsec restoring beam of full-width half-maximum of the MeerKAT image is shown in the bottom left.

The two optical nuclei are highlighted clearly by their emission contours. The northern core is brighter in optical wavelengths. The northern core, which is associated with the radio structure of NGC 326 (Werner, Worrall, and Birkinshaw, 1999), can be seen on the axis of the primary jet. The southern core lies marginally offset from the central jet axis, appears to be a radio core as well and is co-incident with the local brightening of the radio emission. The bright radio emission around the southern core is confined inside the radio jet and any emission outside of the main jet is due to lobe outflows, not originating from the mentioned southern core.

3.4.2 X-ray observations

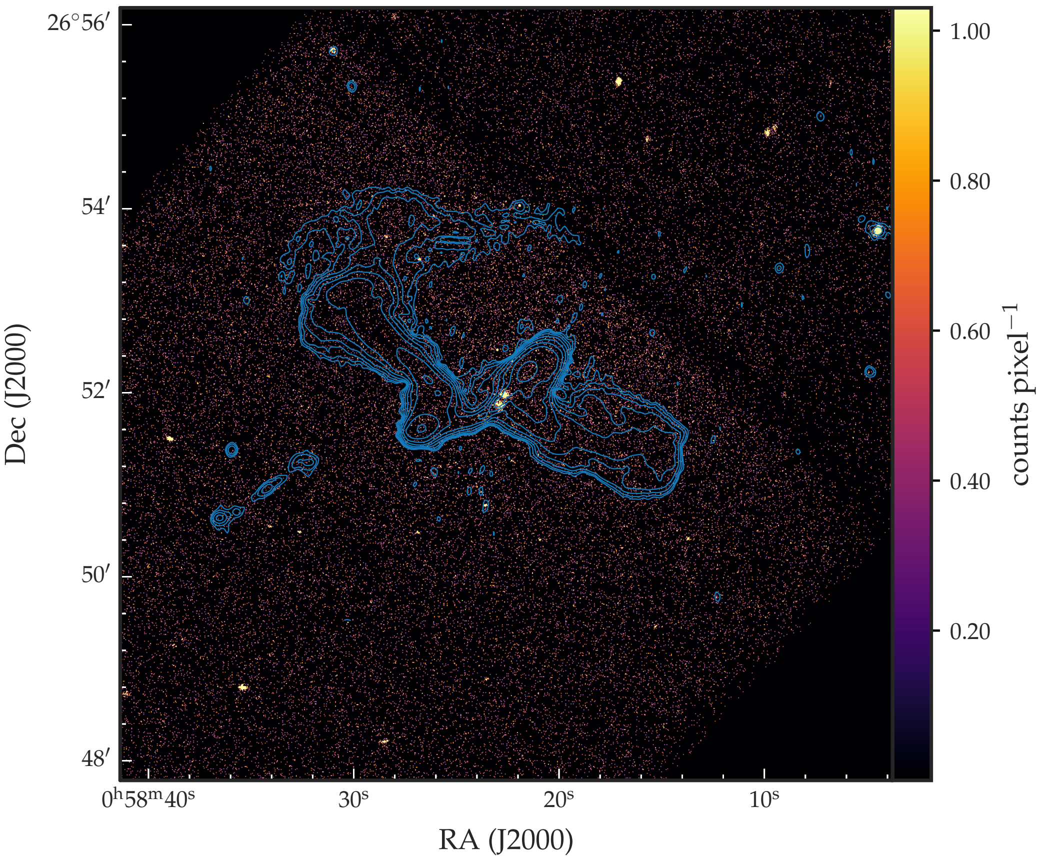

FIGURE 3.12: *Chandra X-ray Observatory* 0.5-7 keV NGC 326 image overlaid by MeerKAT 1.28 GHz contours. The rms noise of the MeerKAT radio data is σ = 19.31 μJy beam^{-1}, and the positive contours are drawn at levels $4\sigma \times 2^0, 2^1, ..., 2^8$ in blue.

We show *Chandra X-ray Observatory* (CXO) images (observation ID 6830) that used the Advanced CCD Imaging Spectrometer (ACIS) from the *Chandra* public archive[8], results of which are first presented in Hodges-Kluck and Reynolds (2012). We did this to better understand and visualise the X-ray emission in the NGC 326 environment in light of our radio data. Figure 3.12 presents the CXO 0.5-7 keV image of NGC 326 with MeerKAT 1.28 GHz contours at levels $4\sigma \times 2^0, 2^1, ..., 2^8$, with σ = 19.31 μJy beam^{-1}. The two nuclei of the dumbbell system can be seen inside the primary jet. Just outside of our dumbbell galaxy, we see a few sources with significant X-ray emission engulfed in radio emission. In the plasma atop the east wing, the X-ray emission associated with galaxy G6 of Werner, Worrall, and Birkinshaw (1999) can be seen. Its radial velocity difference is 1379 km s^{-1} ($2\sigma_z$), and it moves much faster relative to the intra-cluster medium. This has prompted Murgia et al. (2001) to suggest that the association of G6 to the plume is not clear.

On the north-west edge ($\sim 0^h58^m5^s$ 26°54′), MCG 04-03-024 (G5 in Werner, Worrall, and Birkinshaw (1999)) is seen in both X-ray and radio emission. There are other X-ray sources in the north-west without corresponding radio counterparts; whereas in the south-east of NGC 326, radio sources lack X-ray counterparts.

[8] https://cda.harvard.edu/chaser/

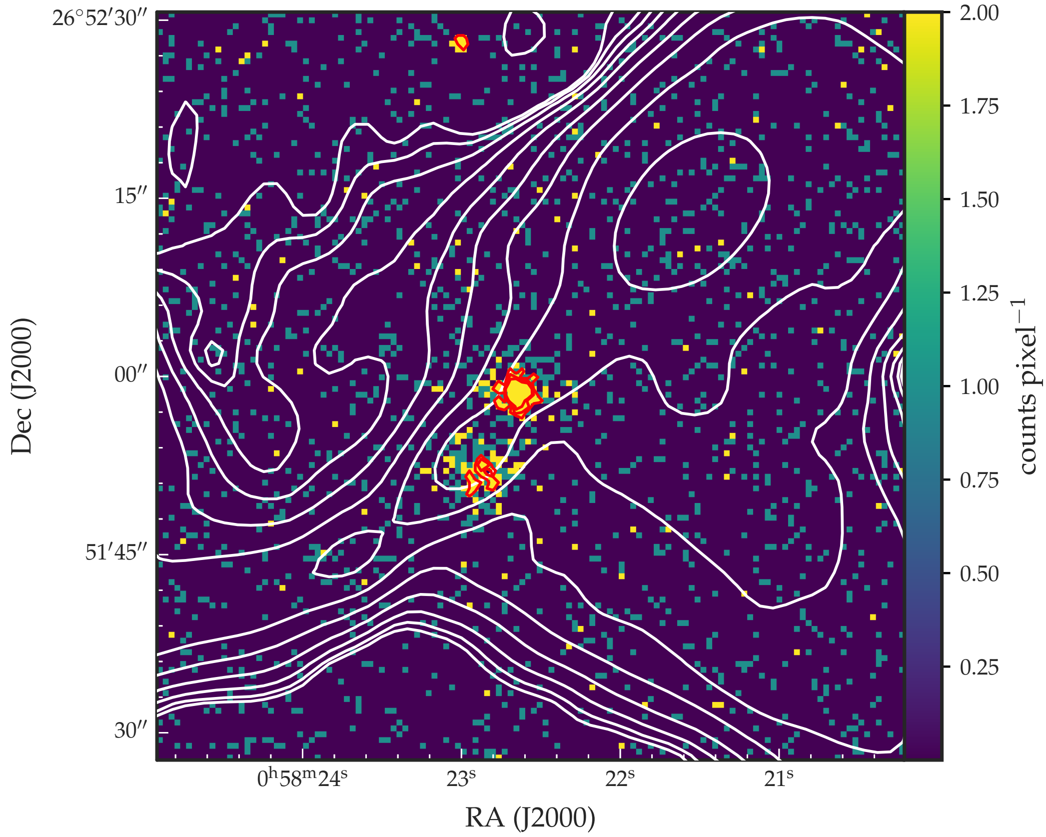

FIGURE 3.13: Zoomed-in *Chandra X-ray Observatory* $0.5-7$ keV image of the central NGC 326 region overlaid by MeerKAT 1.28 GHz contours. The rms noise of the MeerKAT radio data is $\sigma = 19.31$ μJy beam^{-1}, and the positive contours are drawn at levels $4\sigma \times 2^0, 2^1, ..., 2^8$ in white. The red contours are of the CXO data and are drawn at levels 2, 4 and 6 counts pixel^{-1}.

Figure 3.13 is a close-up view of the CXO $0.5-7$ keV data with both MeerKAT and CXO contours overlaid. The northern core resides well in the primary jet whereas the southern core lies slightly off axis of it. Although both nuclei of the system are X-ray emitters, the northern one is more prominent and is responsible for the jet production and the radio structure of NGC 326.

3.5 Radio Spectral Index maps

We created radio spectral index maps of NGC 326 using our new MeerKAT data to help further understand the dynamic and energetics history of the system. The spectral index is a measure of the spectral energy distributions which are characteristic of their radiation (de Gasperin, Intema, and Frail, 2018). It represents the dependence of the radiative flux density on its frequency. As we noted earlier, we will be referring to the spectral index α using the positive convention. Thus,

$$\alpha(\nu) = -\frac{\partial \log S_\nu}{\partial \log \nu}. \tag{3.7}$$

3.5.1 NGC 326 MeerKAT in-band Spectral Index Map

A spectral index map of the galaxy NGC 326 was made using the MeerKAT in-band data. Four of the eight spectral bands, each of bandwidth 107 MHz, were utilised and ranged from a minimum frequency of 1.18 GHz to a maximum 1.60 GHz. The chosen four had the least imaging artefacts out of the total and had a reasonable resolution. The unfortunate trade-off to not using the other spectral bands, particularly those ranging in frequency from 855 MHz to 1177 MHz, was the loss of the faint, extended emission atop the east Wing and a newly identified filamentary feature in the north-east. However, these features lost in the MeerKAT in-band map are present in the MeerKAT–LOFAR spectral index map (Figure 3.15).

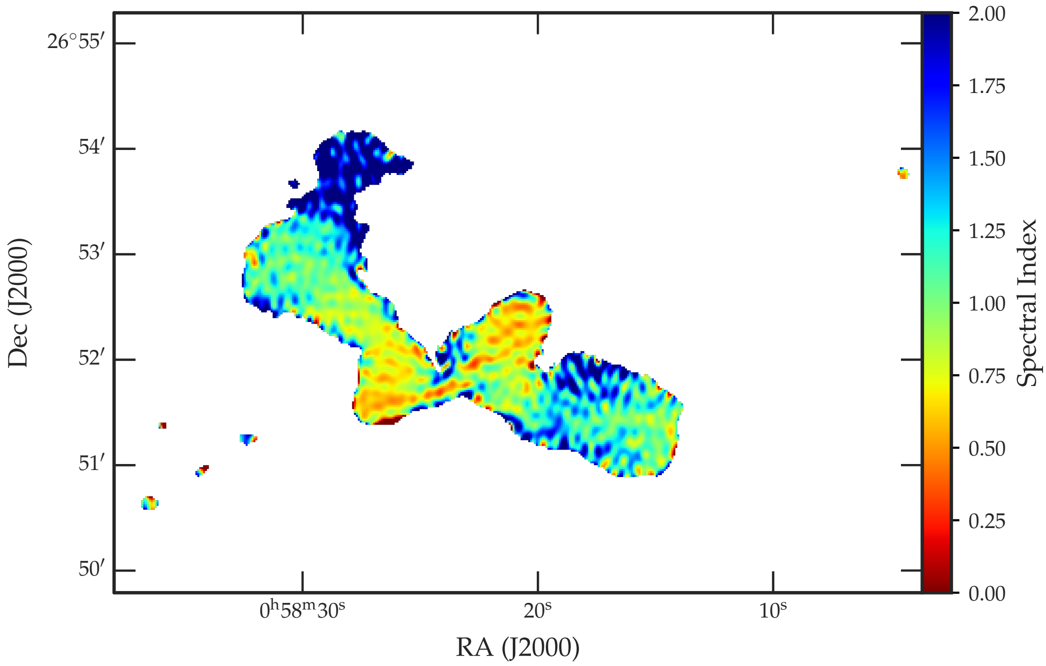

FIGURE 3.14: MeerKAT in-band spectral index map. The map utilised four spectral bands ranging from 1.18 GHz to 1.60 GHz. The colour scale was limited to a spectral index α ranging between $0 - 2$ since most of the data reside in that range. Clear imaging artefacts are still present even in the selected four 'clean' spectral bands.

Figure 3.14 presents the MeerKAT in-band spectral index map of NGC 326. The morphology of this spectral index map is very similar to the NRAO VLA one presented in Figure 4 of Murgia et al. (2001), although with a smaller restoring beam and hence, a better resolution. The lingering imaging artefacts have caused the in-band map to have some anomalous linear features, but general trends can be elucidated nonetheless. A flatter spectral index is observed in the main jets and lobes of the source, ranging mostly around $\alpha \approx 0.3 – 0.7$. As we trace out from the lobes to the wings, we notice that the spectral index steepens to $\alpha \sim 1$. In the east wing, the steepening of the spectral index is more gradual than in the west wing. The spectral index then sharply and dramatically steepens in the plume above the east wing, reaching $\alpha \sim 2$.

3.5.2 NGC 326 MeerKAT–LOFAR Spectral Index Map

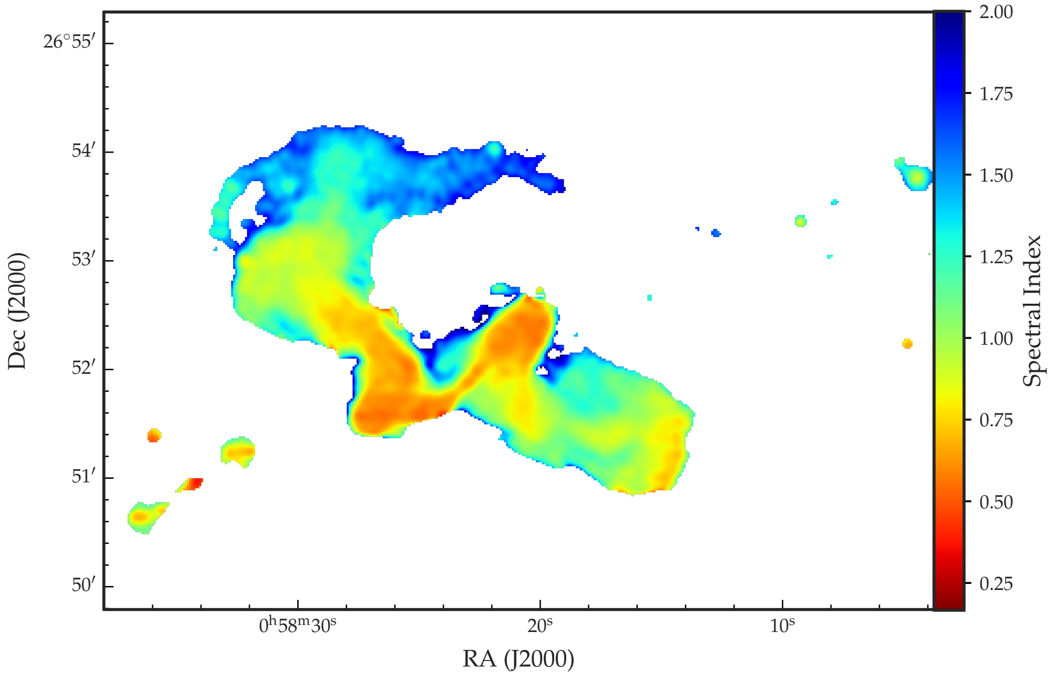

FIGURE 3.15: MeerKAT 1.28 GHz and LOFAR 144 MHz (flux-corrected) spectral index map. The minimum value in the colour scale is set to $\alpha = 0.167$, which is the minimum spectral index in the map, and the maximum is set to $\alpha = 2$.

The MeerKAT–LOFAR spectral index map featured in Figure 3.15 was produced using a multi-frequency synthesis MeerKAT map with a central frequency of 1.28 GHz and a LOFAR map at 144 MHz. Since both these maps have low-frequency data in them compared to the in-band map of Fig. 3.14 (below 1.28 GHz in the MeerKAT map and all data in the LOFAR map), the regions with emission invisible to higher GHz observations is captured properly, as is the spectral index.

Focusing on the main jet, the spectral index α is seen constrained to a small range of $\alpha \sim 0.38 - 0.5$. This flat spectrum is highly collimated at the midsection of the jet and spreads out in the terminating lobes. In the east wing, the spectral index remains flat as the plasma outflows from the lobes into the wing and gradually steepens as it traces up in the wing. The spectral index steepens in the plume at the top of the wing and continues to steepen in the extended emission tracing towards the west. In this MeerKAT–LOFAR map, however, the spectral index in the east wing changes gradually throughout. We also observe an interesting filamentary feature in the north-east part of the wing. It is connected to the top portion of the wing and the north-east 'terminating' part of the secondary jet. Although the spectral index in the top portion is high ($\alpha > 1.50$), the one in the filament is lower at around $\alpha \sim 1.25$.

In the west wing, there are different trends from those observed in the east wing. The change in the spectral index as the plasma outflows from the west lobe is not as gradual as in the east wing. The spectral index rises to ~ 0.75 just as the plasma leaves the lobe. The spectral index continues to rise as we trace out westerly towards the edge of the wing. At the edge of the wing, α flattens from ~ 1.0 to 0.75. Unlike in the east wing, where each cross-section contained almost the same spectral index (with minor exceptions at small sections of the wing), we see a ridge-line of similar spectral index tracing out from the lobe towards the edge of the wing, where it seems to spread out. Taking a cross-section of the west wing, we see that the ridge-line of the 'flatter' spectral index is encapsulated inside a cocoon of plasma with a steeper α. It appears as though the plasma flows inside the collimated ridge towards the edge of the wing, where it spreads out and flows back around the wing towards the main jet.

3.5.3 MeerKAT–LOFAR spectral index with HST contours analysis

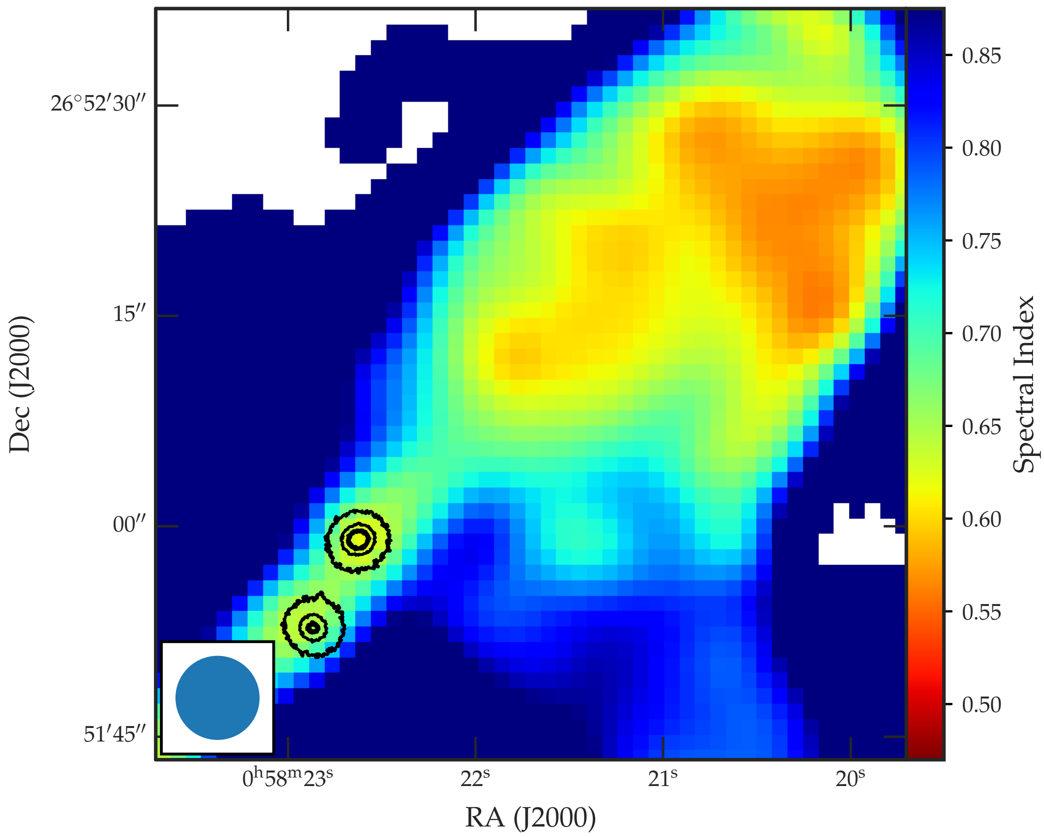

FIGURE 3.16: HST optical cores overlaid onto the MeerKAT–LOFAR spectral index map. With the rms noise being $\sigma = 0.0910$ counts, the contours were drawn at the levels $\sigma \times 2$, 5 and 9. The restoring beam circle of full-width half-maximum of the MeerKAT data is shown in the bottom left.

In the zoomed-in MeerKAT–LOFAR spectral index map presented in Figure 3.16, the HST optical cores are overlaid. The spectral index appears marginally flatter in the vicinity of the cores compared to the jet itself. In the western lobe, the spectral index flattens in the regions where a high flux density was observed, such as in Fig. 3.1.

3.5.4 Radio Spectral Index Profiles

We realise that the spectral index maps are rich in information and require careful analysis. A series of regions with the size of the larger restoring beam of the input images used to create each spectral index map has been drawn. The average spectral index inside each region is carefully extracted from the pixels residing in each region. These averages were used to create spectral index profiles in each region. The errors in our spectral index maps consist of systematic errors calculated using 10% of the absolute flux and the root-mean-square noise in each input image. Using error propagation methods, we then calculated the appropriate resultant error in the spectral index maps. These uncertainties are shown in the spectral index profile plots.

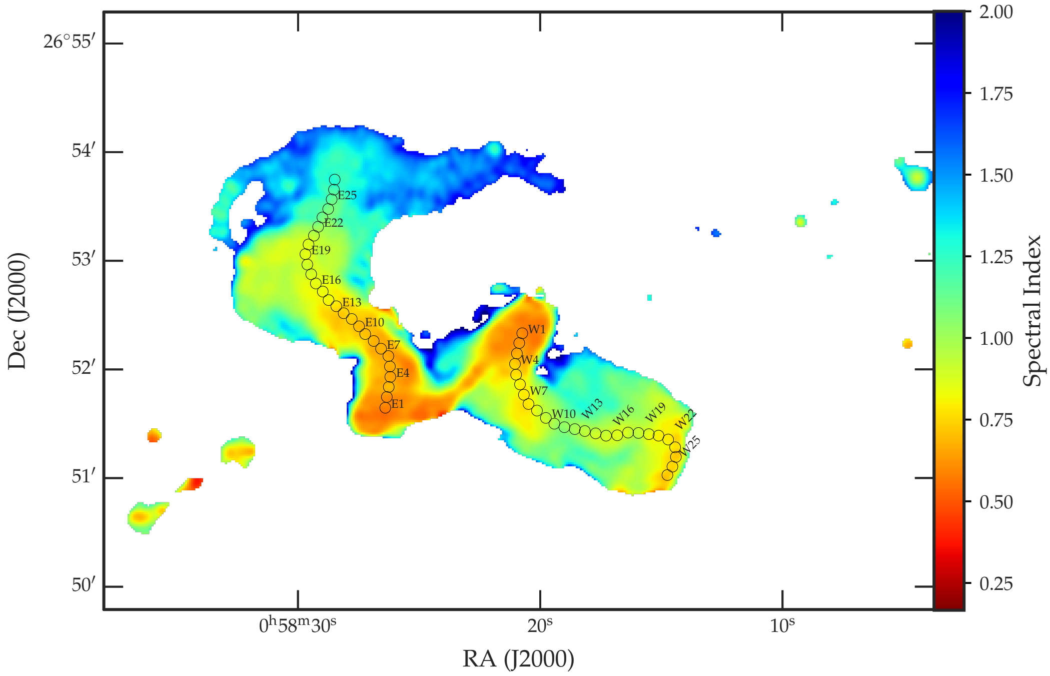

FIGURE 3.17: MeerKAT 1.28 GHz and LOFAR 144 MHz (flux up-scaled) spectral index map with regions along the ridge lines of the east and west wings. The presented regions were used to extract spectral index profiles in the respective regions.

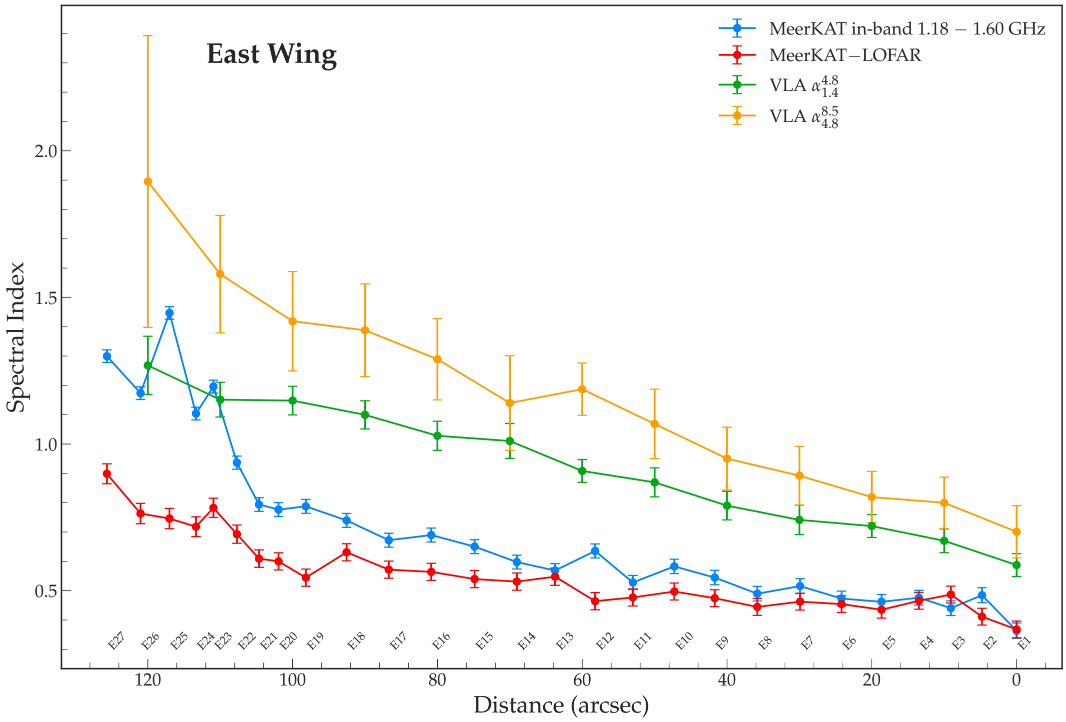

FIGURE 3.18: Spectral index profiles along the east wing ridge lines extracted from the MeerKAT–LOFAR, MeerKAT in-band spectral index maps, and the VLA $\alpha_{1.4}^{4.8}$ and $\alpha_{4.8}^{8.5}$ data were obtained from Murgia et al. (2001). A clear flattening trend is seen across the entire source toward low frequencies. The labels of the regions shown in Fig. 3.17 are included atop the horizontal axis.

The spectral index profiles along the east wing ridge lines of maximum emission are presented in Figure 3.18. For all frequency combinations, we see a monotonically increasing spectral index with distance from the core. The spectral index of higher frequency data is steeper than that of the lower frequencies. Just after region E13, α flattens momentarily before steepening again, for all frequencies. The trend in α after this position is steeper for the VLA $\alpha_{4.8}^{8.5}$ data. The VLA α lines continue to rise without any further deviations. However, the MeerKAT in-band and MeerKAT–LOFAR α lines have perturbations from region E19 onward. This observation is invisible to the VLA data, possibly due to one or more of the following reasons: (1) the size of the regions used in obtaining the spectral index profiles, equal to the resolution of 10″ of the spectral index maps presented by Murgia et al. (2001), is larger than used in our spectral index maps (6″), meaning that smaller disturbances are averaged out in the larger area; (2) the sensitivity and dynamic range of VLA is not good enough to measure the fainter emission, which may contain flatter α; and (3) the radiation in those regions may be dominating at lower frequencies, below the frequency that VLA is observing at. These disturbances are observed in a region in the wing where the plasma is seen spreading out into a larger area. This may also explain why the spectral indices of our data are constant for a few regions. Past that point, the lines all steepen rapidly to higher values.

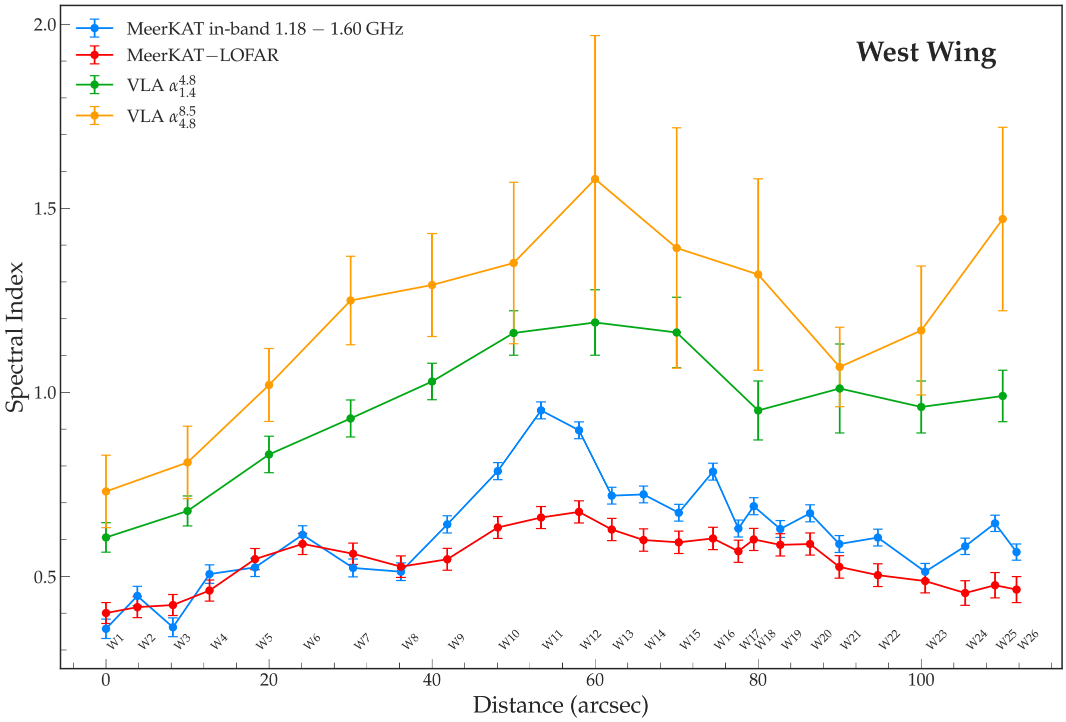

FIGURE 3.19: Spectral index profiles along the west wing ridge lines. The VLA $\alpha_{1.4}^{4.8}$ and $\alpha_{4.8}^{8.5}$ were extracted from Murgia et al. (2001).

The spectral index profiles in the west wing are different from those in the east wing. The spectral indices do not rise monotonically throughout the wing. The obvious similarity here to those of the east wing is those spectral indices of each region are higher for higher frequency data. The α increases overall until region W12. Following the ridge line from W1 to W12, it appears that the plasma outflows from the west lobe and is undisturbed in our line of sight. The substantial flattening in spectral index from region W12 indicates the presence of projection effects at play throughout the west wing – that the outflowing plasma is superimposed with older plasma that has plausibly flowed back from the edge of the wing. The spectral index continues to flatten beyond region W12, with the exception of VLA $\alpha_{4.8}^{8.5}$, where it steepens sharply again from W20. The spectral index remains constant in the last few regions, which is likely a consequence of how the ridge line was drawn. From Figure 3.1 and Figure 3.15, we can conclude that the plasma is perhaps deflected by some 'soft cocoon' at the edge and is spread out around the wing.

We reiterate what we noted earlier: the rate of electron energy loss to synchrotron radiation and the critical frequency for synchrotron emission is proportional to the square of the energy; thus, higher energy electrons are depleted more rapidly, and the source spectra are steepened by synchrotron losses at higher frequencies. This means that older electrons will have a higher spectral index, which may explain why the spectral index in the west wing is so steepened. The newer plasma with lower spectral indices in the west wing is mixed with older plasma with higher spectral indices that have flowed back around the wing, resulting in the observed spectral index profiles having a non-monotonic rise.

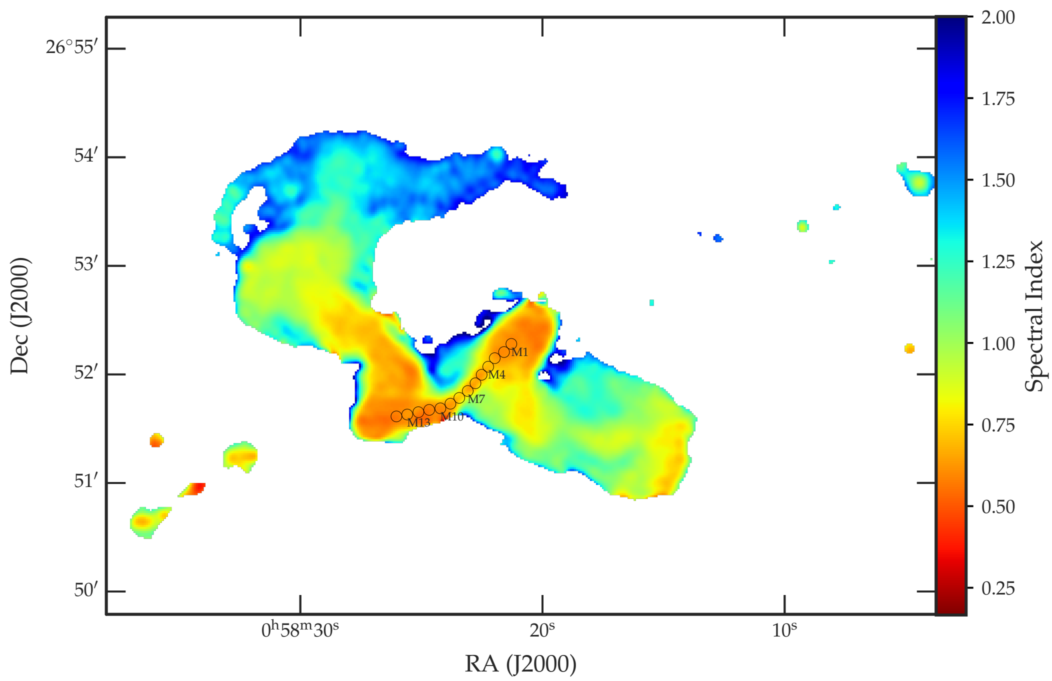

FIGURE 3.20: MeerKAT 1.28 GHz and LOFAR 144 MHz (flux up-scaled) spectral index map with regions along the main jet. The presented regions were used to extract spectral index profiles in the respective regions.

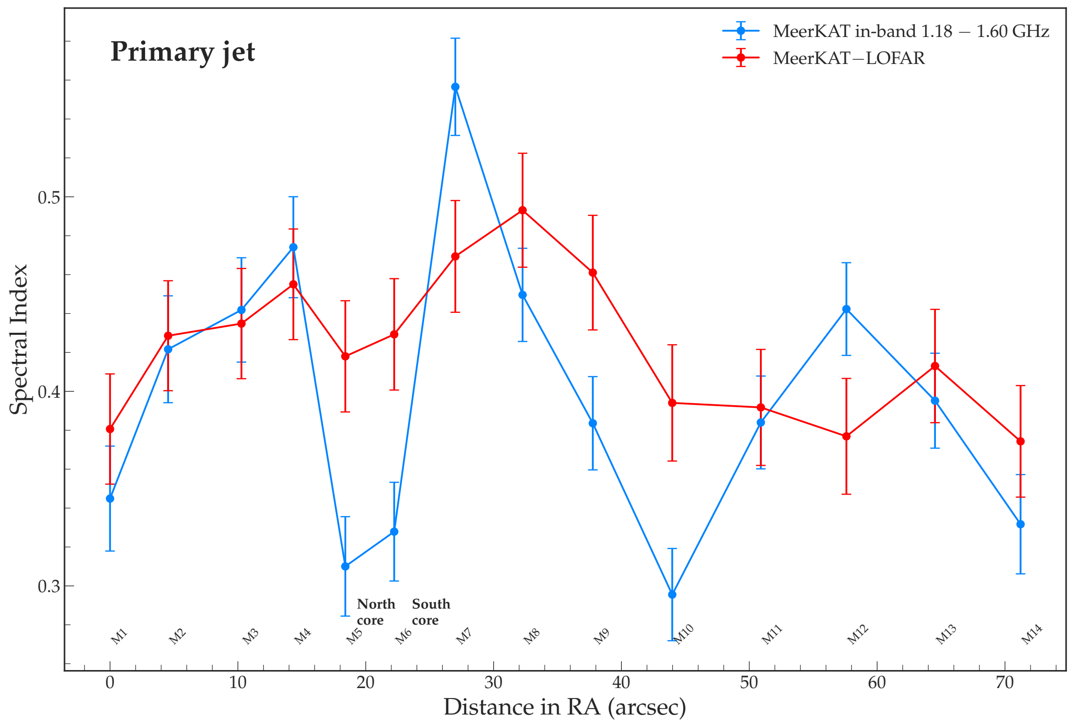

FIGURE 3.21: Spectral index profiles along the main jet. The northern nucleus of NGC 326 resides in regions M5 and M6, and the southern one resides in regions M6 and M7.

The spectral index profiles along the main jet are presented in Figure 3.21. The MeerKAT–LOFAR spectral indices have an average of $\alpha \approx 0.4$ along the main jet. The northern nucleus of the dumbbell galaxy resides in marked regions M5 and M6 while the southern one resides in M6 and M7. The spectral index profiles show little variation along the main jet and remain roughly flat within the margins of the errors. Tracing from region M1, we see that α has an upward trend with a drop around regions M5 and M6, where the cores are located (lower drop for M5 housing the stronger northern core) till it reaches a maximum in the middle of the jet at M8, where the downtrend starts. However, all these trends remain roughly within the error margins, and thus the spectral indices a flat in the primary jet.

As we noted earlier, the MeerKAT in-band spectral index map has anomalous linear features as a result of imaging artefacts related to the input images' spectral bands. This has caused the spectral profiles of the in-band data to be jagged and the trend amplified. However, not all is lost, as we observe that the up and down trends in the in-band spectral index match with those of the MeerKAT–LOFAR. Therefore, the general characteristics of a radio jet and its spectral index can be elucidated.

Chapter 4

Discussion

The discussions of the results presented in Chapter 3 are covered in this chapter. We first look at the innermost regions of the radio galaxy, then we extend our view to discuss the wings and the wing-extension regions. We also incorporate the multi-wavelength data into our discussion and further extend our view to cover the large scale. The role of the spectral indices is also discussed here.

4.1 Inner regions of NGC 326

The source structure in the NGC 326 MeerKAT 1.28 GHz map is complex and projection effects appear to be important. There is an asymmetry in the primary jet, with the host galaxy being closer to the western lobe. Furthermore, the western lobe is larger (in projection) and elongated in the primary jet axis compared to the smaller eastern lobe. Briefly disregarding the northern extension in the east wing, both wings appear relatively symmetric.

Both wings have lower brightness than the primary lobes from which they appear to stem from, and are clearly FR–I type jets. The radio luminosity of the primary jets, including the associated lobes, is 5.3×10^{24} W Hz^{-1} at 1.28 GHz, which lies just below the Fanaroff-Riley luminosity break at that frequency. Compounding this with the fact that the ratio of the (linear) distance between the highest brightness regions on opposite sides of the central galaxy on the primary jet to the total extent of the primary jet measured from the lowest contour is 0.58, just above the 0.5 cutoff, and the lobes being centre-brightened without compact hotspots arguably shows that the immediate environment is sparse enough to allow the weak jets to be FR–II like in some respect. This suggestion has potentially interesting implications for the radio structure which we see today, favouring high bulk growth speeds and the generation of the large and extended wings.

We couple the new observational evidence we have from MeerKAT with what has been reported in the literature to argue that the observed source structure is a result of hydrodynamical backflow. The apparent sharp bends of the lobes into the wings, the radio power of the jets, the hot X-ray medium encapsulating the host galaxy, and the large-scale extension of the source favour the model for hydrodynamical backflow much more than other proposed models.

4.2 Wings and wing-extension regions of NGC 326

The extension of the east wing plasma, which spans ~ 170 kpc at 1.28 GHz in the east-west direction, does not seem to be influenced by any source that is superimposed with the emission. The surface brightness of the east wing extension is an order of magnitude less than that of the east wing itself, which points to fresh plasma–supply intermittency or significantly weaker magnetic field as possible causes. In the west wing, no obvious extension of the wing can be seen in both MeerKAT and LOFAR maps. Given that the host galaxy appears to reside towards the west lobe, and that the west lobe appears elongated in our projection, it is likely that projection effects affect the observed structure of the source, and also likely affect the observed extensions of the wings.

The northeast loop is faint and not well-resolved in our data. Its thin filament-like structure, distinct spectral index, and appearance of connecting two widely separated parts of the east wing suggest that this may be a candidate synchrotron thread, similar to those presented by Ramatsoku et al. (2020). With improved MeerKAT frequency coverage in the future, more about this may be revealed.

4.3 Multi-wavelength data comparison

The VLA 1.4 GHz A+C array map is very similar to the MeerKAT 1.28 GHz map, save for the east wing extension past the plume and the northeast loop in the east wing. While the former is attributable to the VLA's lack of short baselines in A+C array, the latter is surprising, but could be due to MeerKAT's higher dynamic range and imaging fidelity. The asymmetry in the lobes in angular extent, brightness and distance from the core can be seen. The VLA data also reveal the shell-like feature housing the bright emission in the west lobe which has a notable brightness contrast. The same structure cannot be seen in the east lobe, which, as with other features present in the radio structure, could be a consequence of projection effects.

The LOFAR 144 MHz map reveals a larger-scale structure than we observe in our 1.28 GHz data due to their low frequency observation and the steep spectrum of this older plasma. The ~ 3 arcmin east-west tail we see in our data can be seen in the LOFAR map; however, a larger and fainter (by a factor of 10 in surface brightness) tail extension spanning 13 arcmin is exhibited. Hardcastle et al. (2019) argue that the filamentary tail structures provide evidence for large-scale coherent magnetic field enhancements. The formation of the complex large-scale radio structure seems to require a hydrodynamical explanation, which is presumably driven by large-scale bulk motions in the ongoing cluster merger. This is compounded by fact that the host galaxy is also moving with respect to the X-ray-emitting medium. Hardcastle et al. (2019) noted that the formation of the extended tail structure requires either bulk growth speeds much higher than the cluster sound speed for an AGN lifetime of 10^8 years, or a much larger source age.

The overlay of the HST optical contours of the nuclei with the MeerKAT radio data shows that the northern core is the base of the primary jets. The southern core is revealed to have radio emission. Both nuclei are sources of X-ray emission as well. The shell-like structure seen in MeerKAT and VLA maps is revealed to have a high-temperature front in the CXO observation (Hodges-Kluck and Reynolds, 2012).

Whether this structure is a bow shock remains uncertain as there were low counts in the CXO data for temperature deductions. The X-ray emission extends beyond the two nuclei and has been shown to be extensive ($\geq 9'.7 \sim 560$ kpc[1]) and diffuse in the cluster in which the dumbbell galaxy resides.

4.4 Spectral indices

The MeerKAT in-band spectral index map is similar to those of the VLA $\alpha_{1.4}^{4.8}$ and $\alpha_{4.8}^{8.5}$ (as reported by Murgia et al., 2001) in morphology. The pair of primary jets, pair of the wings and the plume atop the east wing are captured. The MeerKAT–LOFAR spectral index map captured the low surface brightness tail extension and the northeast loop. We traced the spectral index along the regions of maximum emission in the wings and found them to behave similarly to the VLA ones presented by Murgia et al. (2001). In the east wing, the behaviour of the spectral index with respect to the distance from the lobe is roughly the same throughout the wing for all frequencies. It steepens in a monotonic fashion. In the west wing, the behaviour is initially monotonic and peaks at a core separation of approximately $50 - 60$ arcsec for all frequencies, after which it flattens. With the observation of the extended tail structures in the MeerKAT and LOFAR observations, the projection effects have been accentuated; thus, we believe projection effects to be at play regarding the flattening of the spectral index in the west wing edge. In addition to this, the flattening of the spectral index at the edge may be a consequence of how the regions were chosen. That is, the regions we drew at the western wing edge are in the same transaxial plane to the wing – showing approximately the same spectral indices.

The spectral index is steeper in the east wing tail, peaking around $\alpha \sim 2$. The rate of electron energy loss to synchrotron radiation and the critical frequency for synchrotron emission is proportional to the square of the energy; thus, higher energy electrons are depleted more rapidly. This is the typical explanation as to why the spectral index is steeper in the tail. However, this assumes similar magnetic field strength and the same effect can be replicated by stronger magnetic fields. As mentioned earlier, Hardcastle et al. (2019) suggested that there could be magnetic field enhancements in a large scale in the tails.

The changes in the spectral index in the primary jet are not as dramatic as in the wings and averages around $\alpha \sim 0.4$. In the primary jet, the spectral index is flatter in the centres of lobes and at locations of the nuclei. This flat spectrum is a result of the plasma in the primary jets being newly ejected and younger than in the rest of the radio source.

[1] Worrall, Birkinshaw, and Cameron (1995) reported a full extent of ≥ 800 kpc at $H_0 = 50$ km s^{-1} Mpc^{-1}.

Chapter 5

Summary and Conclusions

5.1 Summary

In this thesis, we add high-fidelity L-band MeerKAT radio maps to the plethora of imaging performed on NGC 326 across the electromagnetic spectrum. Our spectro-morphological analysis is compared and contrasted with previous observations. The following are some of the primary results and corroborations of this work.

- The extended large-scale structure of the source is revealed for the first time at GHz frequencies, an order of magnitude higher frequency than this steep spectrum emission was discovered at.
- At our angular resolution of 4.8 arcsec, the primary jets and lobes are asymmetric in projected scale, brightness and shape. The radio luminosity of the primary jets is at the transition of the Fanaroff-Riley luminosity break, while the ratio of the distance between high brightness regions on either side of radio core to the primary jets extent is just above the cutoff. Compounding these results with the particular brightness and the shapes of the lobes, these results suggest that the immediate environment may be sparse enough to allow the weak jets to be FR–II like in some respect.
- We derive the spectral index profiles along the wings in the MeerKAT in-band and MeerKAT–LOFAR spectral index maps and compare them to previously published VLA data. For both wings, the spectral index steepens from the lobes towards the edges of the wings – with some peaking and perturbations in the west wing and a monotone behaviour in the east wing. The role of projection effects seems to be of consequence. In the east wing extension, where there is a low surface brightness, a higher spectral index is measured. This is a possible outcome of a population of older and lower energy electrons or the presence of strong magnetic fields in the region.
- The MeerKAT 1.28 GHz total intensity and MeerKAT–LOFAR spectral index maps presented here, as well as the large-scale extensions of the source, offer more support in favour of the hydrodynamical backflow being responsible for the observed source structure. The large-scale extensions of the source, which is moving with respect to the ICM in which it resides, may require a hydrodynamical explanation while their drop in surface brightness compared to the wings seems to imply either fresh plasma-supply intermittency or significantly weaker magnetic fields being possible causes.
- A faint loop in the northeast with a filament-like structure is identified. We suggest that it may be a candidate synchrotron thread based on its spectral index, its thin filamentary structure, and the appearance of connecting two

separate parts of the east wing. We speculate that the hydrodynamical disturbance may potentially play a role in creating such features, together with the large-scale magnetic field structure, however, this will require further, more detailed observations and analysis.

Based on the qualitative assessment of the features present in the map and those of literature, our analysis supports the Hardcastle et al. (2019) argument that hydrodynamical backflow is responsible for the observed source structure. Other proposed models for the formation of X/Z-shaped radio galaxies, such as black hole spin flip or superimposed jets, do not seem to be necessary in explaining the observed radio structure of NGC 326. For instance, the wings being misaligned disfavour the suggestion that they could be a jet and counter-jet pair, as the other models would suggest. As with the large-scale extensions of the source, we argue that the apparent sharp bends (with smooth spectral index transitions) of the lobes into the wings are also a result of hydrodynamical backflows. The optical envelope around the nuclei which also emits X-rays could have deflected the lobe backflows into the wings we see today.

A black hole – black hole merger is not ruled out by our data; however, it appears a more prosaic cause may produce the complex structure which we observe. While this may be true of this particular system, it does not rule out supermassive black hole mergers as a mechanism for abrupt changes in the radio jet axis.

5.2 Prospects

In a project called MeerKAT Extension, additional Square Kilometer Array (SKA) antennas will be added to the MeerKAT telescope which, amongst multiple other improvements in telescope characteristics, will result in increased resolution, imaging fidelity, sensitivity and coverage at higher frequencies at the S-band. With this, the candidate synchrotron thread observed in the east wing may be resolved and possibly uncover how it and similar threads are formed.

Our additional prospects for the future include: probing the magnetic fields around the radio source; determining the source age; and elucidating the spectral index of the radio structure, with a focus on the threads, using what will be new radio data from the aforementioned improved MeerKAT. Detailed, multi-band imaging of nearby universe X-shaped sources such as this will directly assist in discerning the relevant physical drivers of the increasing number of exotic radio source morphologies being identified in SKA precursor and pathfinder surveys.

Bibliography

Abell, George O., Jr. Corwin Harold G., and Ronald P. Olowin (1989). "A Catalog of Rich Clusters of Galaxies". In: *The Astrophysical Journal Supplement Series* 70, p. 1. DOI: 10.1086/191333.

Adams, David J et al. (2004). *An introduction to galaxies and cosmology*. Cambridge University Press.

Antonucci, Robert (1993). "Unified models for active galactic nuclei and quasars." In: *Annual Review of Astronomy and Astrophysics* 31, pp. 473–521. DOI: 10.1146/annurev.aa.31.090193.002353.

Battistini, P. et al. (1980). "The orientation of radiosources associated with elliptical galaxies". In: *Astronomy & Astrophysics* 85.1-2, pp. 101–105.

Bernhard, E. et al. (2016). "An enhanced fraction of starbursting galaxies among high Eddington ratio AGNs". In: *Monthly Notices of the Royal Astronomical Society* 460.1, pp. 902–916. DOI: 10.1093/mnras/stw973. arXiv: 1604.06455 [astro-ph.GA].

Blandford, Roger, David Meier, and Anthony Readhead (2019). "Relativistic Jets from Active Galactic Nuclei". In: *Annual Review of Astronomy and Astrophysics* 57, pp. 467–509. DOI: 10.1146/annurev-astro-081817-051948. arXiv: 1812.06025 [astro-ph.HE].

Booth, R. S. and J. L. Jonas (2012). "An Overview of the MeerKAT Project". In: *African Skies* 16, p. 101.

Briggs, D. S. (1995). "High Fidelity Interferometric Imaging: Robust Weighting and NNLS Deconvolution". In: *American Astronomical Society Meeting Abstracts*. Vol. 187. American Astronomical Society Meeting Abstracts, 112.02, p. 112.02.

Bruni, G. et al. (2019). "A Discovery of Young Radio Sources in the Cores of Giant Radio Galaxies Selected at Hard X-Rays". In: *The Astrophysical Journal* 875.2, 88, p. 88. DOI: 10.3847/1538-4357/ab1006. arXiv: 1903.05922 [astro-ph.GA].

Camilo, F. et al. (2018). "Revival of the Magnetar PSR J1622-4950: Observations with MeerKAT, Parkes, XMM-Newton, Swift, Chandra, and NuSTAR". In: *The Astrophysical Journal* 856.2, 180, p. 180. DOI: 10.3847/1538-4357/aab35a. arXiv: 1804.01933 [astro-ph.HE].

Capetti, A. et al. (2000). "The HST snapshot survey of the B2 sample of low luminosity radio-galaxies: a picture gallery". In: *Astronomy & Astrophysics* 362, pp. 871–885. arXiv: astro-ph/0009056 [astro-ph].

Carilli, C. L. et al. (1991). "Multifrequency Radio Observations of Cygnus A: Spectral Aging in Powerful Radio Galaxies". In: *The Astrophysical Journal* 383, p. 554. DOI: 10.1086/170813.

Cheung, C. C. (2007). "FIRST "Winged" and X-Shaped Radio Source Candidates". In: *The Astronomical Journal* 133.5, pp. 2097–2121. DOI: 10.1086/513095. arXiv: astro-ph/0701278 [astro-ph].

Cheung, C. C. et al. (2009). "First "Winged" and X-Shaped Radio Source Candidates. II. New Redshifts". In: *The Astrophysical Journal Supplement Series* 181.2, pp. 548–556. DOI: 10.1088/0067-0049/181/2/548. arXiv: 0811.3942 [astro-ph].

Condon, James J. and Scott M. Ransom (2016). *Essential Radio Astronomy*.

Cotton, W. D. et al. (2020). "Hydrodynamical backflow in X-shaped radio galaxy PKS 2014-55". In: *Monthly Notices of the Royal Astronomical Society* 495.1, pp. 1271–1283. DOI: 10.1093/mnras/staa1240. arXiv: 2005.02723 [astro-ph.GA].

de Gasperin, F., H. T. Intema, and D. A. Frail (2018). "A radio spectral index map and catalogue at 147-1400 MHz covering 80 per cent of the sky". In: *Monthly Notices of the Royal Astronomical Society* 474.4, pp. 5008–5022. DOI: 10.1093/mnras/stx3125. arXiv: 1711.11367 [astro-ph.IM].

Ehlert, K. et al. (2023). "Self-regulated AGN feedback of light jets in cool-core galaxy clusters". In: *Monthly Notices of the Royal Astronomical Society* 518.3, pp. 4622–4645. DOI: 10.1093/mnras/stac2860. arXiv: 2204.01765 [astro-ph.GA].

Ekers, R. D. et al. (1978). "NGC326 - A radio galaxy with a precessing beam". In: *Nature* 276, pp. 588–590. DOI: 10.1038/276588a0.

Event Horizon Telescope Collaboration et al. (2019). "First M87 Event Horizon Telescope Results. IV. Imaging the Central Supermassive Black Hole". In: *The Astrophysical Journal Letters* 875.1, L4, p. L4. DOI: 10.3847/2041-8213/ab0e85. arXiv: 1906.11241 [astro-ph.GA].

Fabian, A. C. (1999). "The obscured growth of massive black holes". In: *Monthly Notices of the Royal Astronomical Society* 308.4, pp. L39–L43. DOI: 10.1046/j.1365-8711.1999.03017.x. arXiv: astro-ph/9908064 [astro-ph].

— (2012). "Observational Evidence of Active Galactic Nuclei Feedback". In: *Annual Review of Astronomy and Astrophysics* 50, pp. 455–489. DOI: 10.1146/annurev-astro-081811-125521. arXiv: 1204.4114 [astro-ph.CO].

Fanaroff, B. L. and J. M. Riley (1974). "The morphology of extragalactic radio sources of high and low luminosity". In: *Monthly Notices of the Royal Astronomical Society* 167, 31P–36P. DOI: 10.1093/mnras/167.1.31P.

Fernini, Ilias et al. (1993). "Very Large Array Imaging of Five Fanaroff-Riley II 3CR Radio Galaxies". In: *The Astronomical Journal* 105, p. 1690. DOI: 10.1086/116547.

Forman, W., C. Jones, and W. Tucker (1984). "Clusters of galaxies as a probe of the intergalactic medium." In: *The Astrophysical Journal* 277, pp. 19–26. DOI: 10.1086/161666.

Forman, W. et al. (1981). "Einstein imaging observations of clusters with a bimodal mass distribution." In: *The Astrophysical Journal Letters* 243, pp. L133–L136. DOI: 10.1086/183459.

Forman, W. et al. (2010). "3C28 in Abell 115- A Radio Source With a Twist". In: *X-ray Astronomy 2009; Present Status, Multi-Wavelength Approach and Future Perspectives*. Ed. by A. Comastri, L. Angelini, and M. Cappi. Vol. 1248. American Institute of Physics Conference Series, pp. 273–276. DOI: 10.1063/1.3475231.

Garrington, S. T. et al. (1988). "A systematic asymmetry in the polarization properties of double radio sources with one jet". In: *Nature* 331.6152, pp. 147–149. DOI: 10.1038/331147a0.

Gutierrez, K. and H. Krawczynski (2005). "The Off-Axis Galaxy Cluster Merger A115". In: *The Astrophysical Journal* 619.1, pp. 161–168. DOI: 10.1086/426420. arXiv: astro-ph/0312454 [astro-ph].

Hardcastle, M. J. et al. (1997). "High-resolution observations at 3.6cm of seventeen FRII radio galaxies with 0.15<z<0.30". In: *Monthly Notices of the Royal Astronomical Society* 288.4, pp. 859–890. DOI: 10.1093/mnras/288.4.859.

Hardcastle, M. J. et al. (2019). "NGC 326: X-shaped no more". In: *Monthly Notices of the Royal Astronomical Society* 488.3, pp. 3416–3422. DOI: 10.1093/mnras/stz1910. arXiv: 1907.03274 [astro-ph.GA].

Hargrave, P. J. and M. Ryle (1974). "Observations of Cygnus A with the 5-km radio telescope." In: *Monthly Notices of the Royal Astronomical Society* 166, pp. 305–327. DOI: 10.1093/mnras/166.2.305.

Heckman, Timothy M. and Philip N. Best (2014). "The Coevolution of Galaxies and Supermassive Black Holes: Insights from Surveys of the Contemporary Universe". In: *Annual Review of Astronomy and Astrophysics* 52, pp. 589–660. DOI: 10.1146/annurev-astro-081913-035722. arXiv: 1403.4620 [astro-ph.GA].

Heywood, I. et al. (2022). "MIGHTEE: total intensity radio continuum imaging and the COSMOS/XMM-LSS Early Science fields". In: *Monthly Notices of the Royal Astronomical Society* 509.2, pp. 2150–2168. DOI: 10.1093/mnras/stab3021. arXiv: 2110.00347 [astro-ph.GA].

Heywood, Ian (2020). *oxkat: Semi-automated imaging of MeerKAT observations*. Astrophysics Source Code Library, record ascl:2009.003. ascl: 2009.003.

Hodges-Kluck, Edmund J. and Christopher S. Reynolds (2012). "A Chandra Study of the Radio Galaxy NGC 326: Wings, Outburst History, and Active Galactic Nucleus Feedback". In: *The Astrophysical Journal* 746.2, 167, p. 167. DOI: 10.1088/0004-637X/746/2/167. arXiv: 1112.2707 [astro-ph.HE].

Hugo, Benjamin V. et al. (2022). "Tricolour: An Optimized SumThreshold Flagger for MeerKAT". In: *Astronomical Society of the Pacific Conference Series*. Ed. by Jose Enrique Ruiz, Francesco Pierfedereci, and Peter Teuben. Vol. 532. Astronomical Society of the Pacific Conference Series, p. 541. arXiv: 2206.09179 [astro-ph.IM].

Jennison, R. C. and M. K. Das Gupta (1953). "Fine Structure of the Extra-terrestrial Radio Source Cygnus I". In: *Nature* 172.4387, pp. 996–997. DOI: 10.1038/172996a0.

Jonas, J. and MeerKAT Team (2016). "The MeerKAT Radio Telescope". In: *MeerKAT Science: On the Pathway to the SKA*, 1, p. 1. DOI: 10.22323/1.277.0001.

Kenyon, J. S. et al. (2018). "CUBICAL – fast radio interferometric calibration suite exploiting complex optimization". In: *Monthly Notices of the Royal Astronomical Society* 478.2, pp. 2399–2415. DOI: 10.1093/mnras/sty1221. arXiv: 1805.03410 [astro-ph.IM].

Laing, R. A. (1980). "A model for the magnetic-field structure in extended radio sources." In: *Monthly Notices of the Royal Astronomical Society* 193, pp. 439–449. DOI: 10.1093/mnras/193.3.439.

— (1988). "The sidedness of jets and depolarization in powerful extragalactic radio sources". In: *Nature* 331.6152, pp. 149–151. DOI: 10.1038/331149a0.

Laing, R. A. and A. H. Bridle (2002). "Dynamical models for jet deceleration in the radio galaxy 3C 31". In: *Monthly Notices of the Royal Astronomical Society* 336.4, pp. 1161–1180. DOI: 10.1046/j.1365-8711.2002.05873.x. arXiv: astro-ph/0207427 [astro-ph].

— (2014). "Systematic properties of decelerating relativistic jets in low-luminosity radio galaxies". In: *Monthly Notices of the Royal Astronomical Society* 437.4, pp. 3405–3441. DOI: 10.1093/mnras/stt2138. arXiv: 1311.1015 [astro-ph.CO].

Lal, Dharam Vir and A. Pramesh Rao (2005). "3C 223.1: A source with unusual spectral properties". In: *Monthly Notices of the Royal Astronomical Society* 356.1, pp. 232–236. DOI: 10.1111/j.1365-2966.2004.08442.x.

Lalakos, Aretaios et al. (2022). "Bridging the Bondi and Event Horizon Scales: 3D GRMHD Simulations Reveal X-shaped Radio Galaxy Morphology". In: *The Astrophysical Journal Letters* 936.1, L5, p. L5. DOI: 10.3847/2041-8213/ac7bed. arXiv: 2202.08281 [astro-ph.HE].

Landt, Hermine, Chi C. Cheung, and Stephen E. Healey (2010). "The optical spectra of X-shaped radio galaxies". In: *Monthly Notices of the Royal Astronomical Society*

408.2, pp. 1103–1112. DOI: 10.1111/j.1365-2966.2010.17183.x. arXiv: 1006.2179 [astro-ph.CO].

Leahy, J P (1997). *An Atlas of DRAGNs: Glossary*. URL: https://www.jb.man.ac.uk/atlas/gloss.html#flux.

Leahy, J. P. and P. Parma (1992). "Multiple outbursts in radio galaxies." In: *Extragalactic Radio Sources. From Beams to Jets*. Ed. by Jacques Roland, Hilhne Sol, and Guy Pelletier, pp. 307–308.

Leahy, J. P. and A. G. Williams (1984). "The bridges of classical double radio sources." In: *Monthly Notices of the Royal Astronomical Society* 210, pp. 929–951. DOI: 10.1093/mnras/210.4.929.

Lister, M. L. et al. (2019). "MOJAVE. XVII. Jet Kinematics and Parent Population Properties of Relativistically Beamed Radio-loud Blazars". In: *The Astrophysical Journal* 874.1, 43, p. 43. DOI: 10.3847/1538-4357/ab08ee. arXiv: 1902.09591 [astro-ph.GA].

Macklin, J. T. (1983). "Multifrequency radio observations of 3C 28, 76.1, 186 and 319." In: *Monthly Notices of the Royal Astronomical Society* 203, pp. 147–155. DOI: 10.1093/mnras/203.1.147.

Matthews, Thomas A., William W. Morgan, and Maarten Schmidt (1964). "A Discussion of Galaxies Indentified with Radio Sources." In: *The Astrophysical Journal* 140, p. 35. DOI: 10.1086/147890.

Mauch, T. et al. (2020). "The 1.28 GHz MeerKAT DEEP2 Image". In: *The Astrophysical Journal* 888.2, 61, p. 61. DOI: 10.3847/1538-4357/ab5d2d. arXiv: 1912.06212 [astro-ph.GA].

McMullin, J. P. et al. (2007). "CASA Architecture and Applications". In: *Astronomical Data Analysis Software and Systems XVI*. Ed. by R. A. Shaw, F. Hill, and D. J. Bell. Vol. 376. Astronomical Society of the Pacific Conference Series, p. 127.

Merritt, David and R. D. Ekers (2002). "Tracing Black Hole Mergers Through Radio Lobe Morphology". In: *Science* 297.5585, pp. 1310–1313. DOI: 10.1126/science.1074688. arXiv: astro-ph/0208001 [astro-ph].

Mohan, Niruj and David Rafferty (2015). *PyBDSF: Python Blob Detection and Source Finder*. Astrophysics Source Code Library, record ascl:1502.007. ascl: 1502.007.

Murgia, M. et al. (2001). "A multi-frequency study of the radio galaxy NGC 326. I. The data". In: *Astronomy & Astrophysics* 380, pp. 102–116. DOI: 10.1051/0004-6361:20011436. arXiv: astro-ph/0110252 [astro-ph].

NASA/JPL-Caltech (2013). *Black Holes: Monsters in Space (Artist's Concept)*. URL: https://www.jpl.nasa.gov/images/pia16695-black-holes-monsters-in-space-artistsconcept.

Offringa, A. R. et al. (2014). "WSCLEAN: an implementation of a fast, generic wide-field imager for radio astronomy". In: *Monthly Notices of the Royal Astronomical Society* 444.1, pp. 606–619. DOI: 10.1093/mnras/stu1368. arXiv: 1407.1943 [astro-ph.IM].

Perley, R. A. and B. J. Butler (2013). "Integrated Polarization Properties of 3C48, 3C138, 3C147, and 3C286". In: *The Astrophysical Journal Supplement Series* 206.2, 16, p. 16. DOI: 10.1088/0067-0049/206/2/16. arXiv: 1302.6662 [astro-ph.IM].

Planck Collaboration et al. (2016). "Planck 2015 results. XIII. Cosmological parameters". In: *Astronomy & Astrophysics* 594, A13, A13. DOI: 10.1051/0004-6361/201525830. arXiv: 1502.01589 [astro-ph.CO].

Ramatsoku, M. et al. (2020). "Collimated synchrotron threads linking the radio lobes of ESO 137-006". In: *Astronomy & Astrophysics* 636, L1, p. L1. DOI: 10.1051/0004-6361/202037800. arXiv: 2004.03203 [astro-ph.GA].

Readhead, A. C. S. et al. (1978). “Bent beams and the overall size of extragalactic radio sources”. In: *Nature* 276, pp. 768–771. DOI: 10.1038/276768a0.

Rees, M. J. (1966). “Appearance of Relativistically Expanding Radio Sources”. In: *Nature* 211.5048, pp. 468–470. DOI: 10.1038/211468a0.

— (1971). “New Interpretation of Extragalactic Radio Sources”. In: *Nature* 229.5283, pp. 312–317. DOI: 10.1038/229312a0.

Roberts, David H., Lakshmi Saripalli, and Ravi Subrahmanyan (2015). “The Abundance of X-shaped Radio Sources: Implications for the Gravitational Wave Background”. In: *The Astrophysical Journal Letters* 810.1, L6, p. L6. DOI: 10.1088/2041-8205/810/1/L6. arXiv: 1503.02021 [astro-ph.GA].

Spinoglio, Luigi and Juan Antonio Fernández-Ontiveros (2021). “AGN types and unification model”. In: *Nuclear Activity in Galaxies Across Cosmic Time*. Ed. by Mirjana Pović et al. Vol. 356, pp. 29–43. DOI: 10.1017/S1743921320002549. arXiv: 1911.12176 [astro-ph.GA].

Tasse, C. et al. (2018). “Faceting for direction-dependent spectral deconvolution”. In: *Astronomy & Astrophysics* 611, A87, A87. DOI: 10.1051/0004-6361/201731474. arXiv: 1712.02078 [astro-ph.IM].

Valentijn, E. A. and S. Casertano (1988). “Relative velocities of dumbbell galaxies.” In: *Astronomy & Astrophysics* 206, pp. 27–40.

van Marle, A. J., S. P. Owocki, and N. J. Shaviv (2008). “Continuum-Driven Winds from Super-Eddington Stars: A Tale of Two Limits”. In: *First Stars III*. Ed. by Brian W. O’Shea and Alexander Heger. Vol. 990. American Institute of Physics Conference Series, pp. 250–253. DOI: 10.1063/1.2905555. arXiv: 0708.4207 [astro-ph].

Walker, R. Craig et al. (2018). “The Structure and Dynamics of the Subparsec Jet in M87 Based on 50 VLBA Observations over 17 Years at 43 GHz”. In: *The Astrophysical Journal* 855.2, 128, p. 128. DOI: 10.3847/1538-4357/aaafcc. arXiv: 1802.06166 [astro-ph.HE].

Wang, Song et al. (2016). “CHANDRA ACIS Survey of X-Ray Point Sources: The Source Catalog”. In: *The Astrophysical Journal Supplement Series* 224.2, 40, p. 40. DOI: 10.3847/0067-0049/224/2/40. arXiv: 1603.08353 [astro-ph.SR].

Werner, P. N., D. M. Worrall, and M. Birkinshaw (1999). “Redshift and velocity dispersion of the cluster of galaxies around NGC 326”. In: *Monthly Notices of the Royal Astronomical Society* 307.3, pp. 722–724. DOI: 10.1046/j.1365-8711.1999.02677.x. arXiv: astro-ph/9906407 [astro-ph].

Wirth, A., L. Smarr, and J. S. Gallagher (1982). “Dumbbell galaxies and precessing radio jets.” In: *The Astronomical Journal* 87, pp. 401–404. DOI: 10.1086/113135.

Worrall, D. M., M. Birkinshaw, and R. A. Cameron (1995). “The X-Ray Environment of the Dumbbell Radio Galaxy NGC 326”. In: *The Astrophysical Journal* 449, p. 93. DOI: 10.1086/176035.

Yang, Xiaolong et al. (2019). “Extended Catalog of Winged or X-shaped Radio Sources from the FIRST Survey”. In: *The Astrophysical Journal Supplement Series* 245.1, 17, p. 17. DOI: 10.3847/1538-4365/ab4811. arXiv: 1905.06356 [astro-ph.HE].

Zwicky, F. and C. T. Kowal (1968). *“Catalogue of Galaxies and of Clusters of Galaxies”, Volume VI.*